Journal of Offshore Mechanics and Arctic Engineering. Received April 22, 2022;
Accepted manuscript posted August 22, 2022. doi:10.1115/1.4055402

Modal analysis of offshore monopile wind turbine: An analytical solution

Hadi Pezeshki [1]
University of Stavanger, Norway
Kjølv Egelands hus, E block (2nd floor), Kristine Bonnevies vei 22, 4021 Stavanger, Norway
hadi.pezeshki@uis.no

Dimitrios Pavlou
University of Stavanger, Norway
Kjølv Egelands hus, E block (2nd floor), Kristine Bonnevies vei 22, 4021 Stavanger, Norway
dimitrios.g.pavlou@uis.no

Hojjat Adeli
Ohio State University, USA
The Ohio State University, Columbus
adeli.1@osu.edu

Sudath C. Siriwardane
University of Stavanger, Norway
Kjølv Egelands hus, E block (2nd floor), Kristine Bonnevies vei 22, 4021 Stavanger, Norway
sasc.siriwardane@uis.no

ABSTRACT

An analytical solution of the dynamic response of offshore wind turbines under wave load with nonlinear Stokes's wave theory and wave-structure and soil-foundation interactions is developed. Natural frequencies and the corresponding modes are obtained. The effect of the wave-structure interaction, the added mass, the foundation stiffness, and the nacelle translational and rotational inertia on the motion of the structure is investigated. The nonlinear loading provided by the drag term of Morison's equation is successfully handled. A parametric study to examine the effect of the structural parameters on the dynamic response is conducted and the results of the proposed analytical solution are compared to numerical ones. The proposed method has the following advantages: a) it is accurate and straightforward because of its analytical nature, b) it does not ignore the drag term in the wave loading by keeping its nonlinearity nature, c) the structure of the wind turbine is modeled as a continuous system, d) it takes into account the effect of the rotational and translational inertia of the nacelle on the dynamic response, e) it provides an interpretation of the effect of the sea level variation in changing the natural frequencies.

Keywords: Offshore Wind Turbine, Response, Natural frequencies, Natural modes, Wave-Structure interactions, Nonlinear wave kinematics, Soil-Structure Interactions.

[1] Corresponding author information can be added as a footnote.

Journal of Offshore Mechanics and Arctic Engineering. Received April 22, 2022;
Accepted manuscript posted August 22, 2022. doi:10.1115/1.4055402

1. Introduction

Passing from carbon-emission to carbon-neutral energy sources motivates many countries to invest in renewable energies. Among them, offshore wind turbines (OWTs) have been chosen as the main source of renewable energy for many European countries [1]. Being installed in the offshore and nearshore mostly by fixed support structures poses challenges in optimum designing. Furthermore, the prediction of the long-term structural behavior of these structures required for structural integrity assessment is not available because the majority of the OWTs have been installed in the past ten years, and the data acquisition is very costly.

OWTs are subjected to coupled dynamic phenomena due to the interaction of wind and wave loads and the rotor's vibration. Therefore, dynamic stability and vibration control [2,3] is a topic that attracts the attention of researchers. Pioneering works on vibrational control of large real-life structures under dynamic loading have been performed by Adeli and Saleh [4–7]. Reviews of advances in vibration control algorithms for smart structures up to 2017 are presented by [8–10]. Since the coupling phenomena are complicated to be modeled by regular deterministic techniques, Machine Learning (ML) algorithms seem to be a promising alternative tool. Adeli and associates developed intelligent control algorithms employing neural networks and ML techniques as far back as 2008 [11,12]. More recent work on intelligent control of large real-life buildings and bridge structures was presented by [9,13–19] to discuss and advance the novel concept of integration of vibration control, health monitoring of structures [20,21] and energy harvesting [22] for smart cities of the future.

A key technology in the field of structural engineering in recent years has been automated structural health monitoring (SHM). There are two fundamentally different approaches to SHM, one based on vibration [23] and the other based on imaging and computer vision [24]. Vibration-based SHM technology requires adroit integration of vibration theory, signal processing such as wavelets [25], and machine learning [26,27]. SHM technology has been used successfully and there is a significant body of research on health monitoring of building structures and bridges [28], dams [29], railways [30], pavements [31], retaining structures along highways [32], and tunnels [33], but little work has been reported on health monitoring of offshore structures and wind turbines. A method of vibration-based SHM is based on computing and monitoring the structural properties such as natural frequencies and mode shapes [34]. Besides, the remaining fatigue life is also necessary to be evaluated and monitored in the case of offshore structures. One of the main challenges in fatigue life estimation, apart from selecting a novel accumulating damage model [35–37], is the availability of the stress history resulting from dynamic response of the structure in the hot spots.

The stress history required for fatigue life evaluation can be obtained from two main sources. One source would be simply by measuring the stress history of the real operating structure. Although the field data is extremely valuable because it reflects the real behavior of the structure, harvesting field data is expensive and in some cases, impossible. An alternative source would be generating data through the mathematical models by simulating the real operating situation. An immediate method in providing the response or stress history of an OWT structure, including all its complexities, is to utilize the numerical models by discretizing the structure via finite elements

Journal of Offshore Mechanics and Arctic Engineering. Received April 22, 2022;
Accepted manuscript posted August 22, 2022. doi:10.1115/1.4055402

methods. Many researchers [38–48] are using commercial software packages or numerical platforms to simulate these structures due to their accessibility and ability to create high-fidelity models. However, numerical solutions are still time-consuming, and their performance is affected by stability issues especially in very complicated time domain problems. The other alternative to generating response data is to develop the analytical solutions to achieve the response as a single function by which the response is evaluated for arbitrary loading parameters. Analytical solutions are straightforward, provide always-true and reliable results as opposed to the numerical ones but challenging to achieve because of complex mathematics.

Unlike a large number of existing numerical models, very few analytical models of the OWTs have been published. Scientists such as Graff [49] and Meirovitch [50] started early works on the classical methods of solving the wave equation in a cantilever flexural beam in the 60s and 70s. They introduced some methods for solving these equations. For instance, Graff [49] listed five methods: 1) Finite Fourier transform, 2) Expansion in the natural modes (in the spatial domain), 3) Laplace transform, 4) Laplace transform-natural mode expansion, and 5) solution by the natural modes (in both spatial and temporal domain). In the first two methods, it is assumed that the solution contains two separate parts in time and space. While for the last three ones, the solution begins directly from the equation of motion with an arbitrary function. Among these methods, expansion in the natural modes relies on the structure's natural modes, which can be found from the homogeneous form of the equation of motion with respect to its boundary conditions. This method also provides the result in the form of a single function as apposed to numerical solutions where a set of numbers is obtained as the response. Expansion in the normal modes is also flexible in the external load situations. Complex loading can be expanded by using the Fourier series and analyzed. Selecting other methods requires more effort, and sometimes impossible to find the solution. For instance, the method of Laplace transforms requires inverse Laplace transform, which is nearly impossible to be determined analytically for complicated boundary conditions. Pavlou [51] developed an analytical solution for the evaluation of the response of the OWT under the linear waves. In this work, the translational and rotational inertial effect of the nacelle, the hydrodynamic damping, and the soil-foundation interaction have been analytically investigated for gravity-based supported structures. The achieved analytic inversion of Laplace Transforms was very challenging in this analysis. Apart from mentioned methods, very few analytical solutions have been proposed in the past years. In a rare case, Wang et al. [52] developed a mathematical model for dynamic analysis of an onshore wind turbine by using the thin-walled theory [45,53–55] to simulate the comprehensive behavior of the wind turbine.

Expansion of the response in the natural modes requires having an accurate and reliable estimation of the natural frequencies of the OWT structure. In the past few years, researchers have attempted to provide models in which the realistic situation of an OWT is included. Most of the works have been focused on the soil and foundation situation. In a study conducted by Arany et al. [56], an analytical model was developed by simulating foundation flexibility using three springs. The effect of boundary conditions on the natural frequencies has been parametrically studied by defining some non-dimensional parameters. Having compared the analytical natural frequencies with the measured ones from the actual OWTs, a slight inaccuracy was reported, which is not improved by modeling the tower with the Timoshenko beam theory. In another study, They [57] proposed a simplified methodology to have a quick hand calculation of the 1st

Journal of Offshore Mechanics and Arctic Engineering. Received April 22, 2022;
Accepted manuscript posted August 22, 2022. doi:10.1115/1.4055402

natural frequency of an OWT. In their works, the effect of the fluid-structure interactions of the added mass has not been considered, which may be the reason for the inaccuracy they have reported. Bouzid et al. [58] established a nonlinear finite element model [59] to obtain the head stiffness of the monopile support structure at the mudline. Their purpose was to improve the accuracy of the results obtained by Arany et al. [56,57]. Recently, Alkhoury et al. [60] established a full 3D model for the DTU 10 MW OWT including all the details of the nacelle, blades, rotor, as well as full 3D modeling of the soil inside and outside of the monopile and cross-sectional variation of the tower structure. More details about this work will be presented later in this paper for the sake of verification.

The natural frequencies of the OWT were also measured in the real-operating systems. Damgaard et al. [61] have reported the cross-wind modal properties of an OWT. They have reported that the 1st natural frequency is time-dependent which might be because of erosion of the soil around the monopile or soil scouring. Later, variation of the natural frequency in time attracts the attention of Prendergat et al. [62,63], resulting in two publications. In their first work [62], the scouring effect on the natural frequency was investigated without considering the effect of added mass in the system. In their second work [63], however, they considered other factors such as water added mass influencing the dynamic properties of the system. Another investigation on the measured data conducted by Dong et al. [64] also reported the time-dependent dynamic properties of an OWT. Moreover, a precise analysis was performed on the measured data by Cosgriff et al. [65]. The 1st natural frequency was separately plotted versus the wave height and wind speed based on 20 min measured data in the calm sea condition while the wind velocity was under the cut in speed. The trend reveals that the 1st natural frequency is reduced as the wave height and wind speed increase. This phenomenon raises suspicion about the effect of added mass on the natural frequencies by sea level variation.

Attempts toward providing an accurate response require accurate and realistic inputs in the analysis alongside accurate and realistic models and solutions. In the case of bottom-fixed OWTs which are mostly installed in shallow to intermediate water depth, measurements and studies reveal that nonlinear wave theory should be implemented to simulate the realistic sea states. A study conducted by Natarajan [66] showed that using the 2nd order wave theory significantly increases the extreme loading on the monopile support structure of OWTs. Yingguang Wang [67] utilized a transformed linear method to simulate the 2nd order irregular wave to obtain the wave load by including the sea bottom effect. Shaofeng Wang et al. [68] conducted a case study to investigate the ultimate wave loads on a 10 MW OWT. All of them have reported a significant increase in wave load on the structure.

In the present work, a new analytical solution for modal analysis of OWT structures is presented. Nonlinear waves and wave-structure and soil-foundation interactions are accounted for in the solution. The consideration of the 2nd nonlinear wave kinematics improves the ability of the method to cover a higher range of wavelength and height, providing more realistic loading on the structure. OWTs are subjected to different types of environmental loading such as wind, waves, ocean currents, earthquakes, ship collisions, etc [69]. Among them, dealing with the wave loads is still a challenging task due to its complexities and uncertainties [70]. Therefore, this study focuses on the wave load. Moreover, the analytical modeling of the translational and rotational inertia effect of the nacelle and the fluid-structure and soil foundation interaction improves the

Journal of Offshore Mechanics and Arctic Engineering. Received April 22, 2022;
Accepted manuscript posted August 22, 2022. doi:10.1115/1.4055402

reliability of the dynamic simulation. The novelty of the presented work beyond the published literature is based on the following advantages: The solution is accurate and straightforward because of its analytical nature, it does not ignore the drag term in the wave loading, the structure of the wind turbine is modeled as a continuous system by including its geometrical discontinuities, it takes into account the effect of the rotational and translational inertia of the nacelle, and it provides an interpretation of the effect of the sea level variation on the natural frequencies. The research presented in this paper can be extended for health monitoring of offshore structures and wind turbines which is intended as part of future research by the authors.

2. Formulation of the problem

A typical horizontal axis OWT consists of nacelle and blades systems mounted on the top of a tower fixed to the seabed by a monopile, as illustrated in Figure 1-a. A transition part connects the tower and monopile at sea level. In this paper, an OWT is modeled as a cantilever column supported by a set of springs at one end and free at the other end, see Figure 1-b. This cantilever beam, which is called the system for the rest of this paper, consists of two parts separated from the platform level at the top of the transition part. This is because their dimensions and properties can be significantly different. The cross-sectional properties of each part are assumed constant. The symbols definition used in this paper is represented in Table 1. The monopile under the seabed is also modeled by a set of four springs representing the lateral, rotational, cross-coupled, and vertical stiffnesses with constants of K_L, K_R, K_{LR}, K_z, respectively [71].

In this study, the motion of the system is considered as a lateral deflection due to the wave load applied up to Mean Sea Level (MSL). As shown in Figure 1-c, the deflection, $x(z,t)$, is defined as a continuous function of time, t, and space, z, implying to represent the motion of the system with an infinite degree of freedom.

2.1. The governing equation

For the system introduced in Figure 1-c, the Bernoulli-Euler beam theory can be applicable for small displacements [49]. Therefore, the equation of motion along the height of the system with the origin from the seabed can be written as

$$EI(z)\, x^{(iv)}(z,t) + \mathrm{M(z)}\ddot{x}(z,t) = q(z,t)\, H_3(z) \quad (1)$$

where, $q(z,t)$ is the external forces acting perpendicular to the monopile's longitudinal axis. $EI(z)$ and $M(z)$ are the flexural rigidity and mass per unit length of the system. For the system defined in Figure 1, they are defined as follows:

$$M(z) = m_{Tow}\, H_1(z) + m_{Mon}H_2(z) + m_{Mon}H_3(z) \quad (2)$$

$$EI(z) = EI_{Tow}H_1(z) + EI_{Mon}H_2(z) + EI_{Mon}H_3(z) \quad (3)$$

Where $H_i(z), i = 1, 2, 3$ are the step functions defined as

Journal of Offshore Mechanics and Arctic Engineering. Received April 22, 2022;
Accepted manuscript posted August 22, 2022. doi:10.1115/1.4055402

$$H_1(z)=\begin{cases}1, & for\ L_{Plat}\leq z\leq L\\ 0, & for\ d<z\leq L_{Plat}\\ 0, & for\ 0<z\leq d\end{cases} \tag{4}$$

$$H_2(z)=\begin{cases}0, & for\ L_{Plat}\leq z\leq L\\ 1, & for\ d<z\leq L_{Plat}\\ 0, & for\ 0<z\leq d\end{cases} \tag{5}$$

$$H_3(z)=\begin{cases}0, & for\ L_{Plat}\leq z\leq L\\ 0, & for\ d<z\leq L_{Plat}\\ 1, & for\ 0<z\leq d\end{cases} \tag{6}$$

For a slender structure, Morison's equation from [72,73] can be adopted for dynamic modeling. Also, the relative velocity formulation is applicable for a moving slender structure subjected to the wave loads. Since the bottom-fixed support structure is of interest, it is expected that the underwater motion of the system to be way below its diameter. Therefore, the relative velocity in the drag term can be reduced to the wave horizontal particle velocity. For an ocean wavelength larger than five times the monopile diameter and the small displacement, the wave load on the monopile can be represented by the relative velocity formulation [72] as

$$q(z,t)=-\rho_w C_A A_{Mon}\ddot{x}(z,t)+\rho_w C_M A_{Mon}\frac{Du(z,t)}{Dt}+\frac{1}{2}\rho_w C_D D_{Mon}u(z,t)|u(z,t)| \tag{7}$$

In equation (7), the two first terms inside the curl bracket are inertial and the third one is the drag term. The total derivative of the wave horizontal particle velocity, $Du(z,t)/Dt=\partial u/\partial t+u\,\partial u/\partial x+w\,\partial u/\partial z$, in the inertial term can be reduced to $\dot{u}(z,t)=\partial u(z,t)/\partial t$ by neglecting the advocative terms which are reported to slightly increase the load when they are included [70]. The inertia term reveals that the $-\rho_w C_A A_{Mon}\ddot{x}(z,t)$ provides an additional mass to the system affecting its oscillating properties. This added mass can represent itself in the equation of motion, Eq. (1). By substituting Eq. (7) into Eq. (1) the result will be

$$x^{(iv)}(z,t)+\mathrm{A}(z)\ddot{x}(z,t)=\frac{1}{EI_{Mon}}Q(z,t)\,H_3(z) \tag{8}$$

where

$$A(z)=\frac{1}{a_{Tow}^2}H_1(z)+\frac{1}{a_{\mathrm{MA}}^2}H_2(z)+\frac{1}{a_{MU}^2}H_3(z) \tag{9}$$

$$a_{\mathrm{Tow}}^2=\frac{EI_{Tow}}{m_{Tow}} \tag{10}$$

$$a_{\mathrm{MA}}^2=\frac{EI_{Mon}}{m_{Mon}} \tag{11}$$

$$a_{\mathrm{MU}}^2 = \frac{EI_{Mon}}{m_{Mon} + \rho_w C_A A_{Mon}} \tag{12}$$

$$Q(z,t) = \rho_w C_M A_{Mon} \dot{u}(z,t) + \frac{1}{2}\rho_w C_D D_{Mon} u(z,t)|u(z,t)| \tag{13}$$

Eq. (8) represents a partial differential equation governing the motion of the system subjected to the wave load. The added mass is included on the right side of the equation. Thus, the left side is not dependent on the motion of the tower. Parameter a_{MU} are containing the mass of the system underwater including added mass. Therefore, the wave-structure interaction is included in the equation of motion.

It can be seen in Eq. (8) that there are three separate systems, the tower, monopile above water and monopile underwear, acting together to govern the motion of the system. Therefore, it can be separated in the form of three independent equations as

$$x_{Tow}^{(iv)}(z,t) + \frac{1}{a_{Tow}^2}\ddot{x}_{Tow}(z,t) = 0, \qquad for\ L_{Plat} \le z \le L \tag{14}$$

$$x_{MA}^{(iv)}(z,t) + \frac{1}{a_{MA}^2}\ddot{x}_{MA}(z,t) = 0, \qquad for\ d < z \le L_{Plat} \tag{15}$$

$$x_{MU}^{(iv)}(z,t) + \frac{1}{a_{MU}^2}\ddot{x}_{MU}(z,t) = \frac{1}{EI_{Mon}}Q(z,t), \qquad for\ 0 < z \le d \tag{16}$$

In the three above equations $x_{Tow}(z,t)$, $x_{MA}(z,t)$ and $x_{MU}(z,t)$ stand for the lateral motion of the system in the tower, monopile above water and underwater, respectively. Eq. (14) and (15) are homogeneous partial differential equations implying that the motion above water is a kind of free vibration whereas the underwater motion, represented in Eq. (16), is a forced vibration due to the external load. Therefore, the above water motion is activated by the motion of the underwater part via a series of boundary conditions which will be introduced later.

2.2. The boundary and initial conditions

To accommodate the motion of the system with the equation of motion in Eq. (8), two sets of conditions at the two ends of the system are needed. The motion of the system at the seabed is governed by a set of 4 springs as illustrated in Figure 1-b. Vertical stiffness, K_z, can be neglected because the vertical motion of the system is negligible. The three remaining springs can be collected in the matrix form to obtain the shear force, F, and bending moment, M, at the seabed by the following equation [71]:

$$\begin{bmatrix} F(t) \\ M(t) \end{bmatrix} = \begin{bmatrix} K_L & K_{LR} \\ K_{LR} & K_R \end{bmatrix} \begin{bmatrix} x(0,t) \\ x'(0,t) \end{bmatrix} \tag{17}$$

By substituting the shear force and bending moment from the beam theory into the above equation and expanding, it yields to the following two boundary conditions.

$$-EI_{Mon}\,x'''_{MU}(0,t) = \mathrm{K}_L x_{MU}(0,t) + K_{LR}x'_{MU}(0,t) \tag{18}$$

$$EI_{Mon}\,x''_{MU}(0,t) = K_{LR}x_{MU}(0,t) + \mathrm{K_R}\,x'_{MU}(0,t) \tag{19}$$

At the top of the tower, a heavy nacelle is mounted providing lump mass to the system. The effect of the translational and rotational inertia of the mass of the nacelle can be simulated as the two following conditions:

$$-EI_{Tow}\,x''_{Tow}(L,t) = J_P\ddot{x}'_{Tow}(L,t) \tag{20}$$

$$EI_{Tow}\,x'''_{Tow}(L,t) = M_N\ddot{x}_{Tow}(L,t) \tag{21}$$

The rotational motion of the nacelle produces the momentum proportional to the tower's rotational acceleration $\ddot{x}'_{Tow}(L,t)$ at the top of the system which should be in equilibrium with the total moment of the system producing boundary condition in the form of Eq. (20). Besides, the translational acceleration of the nacelle, $\ddot{x}_{Tow}(L,t)$, creates an inertial force that should be equal to the internal shear force of the tower at the nacelle level. This equilibrium is represented by Eq. (21).

As mentioned earlier, the two Eqs. (15) and (16) govern the motion of the monopile. Therefore, it is necessary that these equations are linked together at the sea level via some boundary conditions. They are

$$x_{MU}(d,t) = x_{MA}(d,t) \tag{22}$$

$$x'_{MU}(d,t) = x'_{MA}(d,t) \tag{23}$$

$$x''_{MU}(d,t) = x''_{MA}(d,t) \tag{24}$$

$$x'''_{MU}(d,t) = x'''_{MA}(d,t) \tag{25}$$

Also, Eqs. (14) and (15) are connected by following boundary conditions

$$x_{MA}(L_{Plat},t) = x_{Tow}(L_{Plat},t) \tag{26}$$

$$x'_{MA}(L_{Plat},t) = x'_{Tow}(L_{Plat},t) \tag{27}$$

$$EI_{Mon}x''_{MA}(L_{Plat},t) = EI_{Tow}x''_{Tow}(L_{Plat},t) \tag{28}$$

$$EI_{Mon}x'''_{MA}(L_{Plat},t) = EI_{Tow}x'''_{Tow}(L_{Plat},t) \tag{29}$$

The last eight boundary conditions are based on the system's continuity on deflection and slope of the motion at sea level as well as the internal shear force and bending moment continuity of the system at a point where two systems are linked together.

It is assumed that the tower motion starts from the position when it is at the rest. Therefore, the initial deflection and the velocity of each part of the tower are zero. It yields to the following initial conditions

$$x(z,0) = \dot{x}(z,0) = 0 \tag{30}$$

3. Solution for the equation of motion

The method that has been chosen to solve Eq. (8) is to expand the response in the natural modes of the system. The natural frequencies of the system and consequently the natural mode shapes will be obtained. Then, they will be utilized in the solution for the forced vibration.

3.1. Natural modes

The natural modes will be evaluated by using the homogenous form of Eq. (16) as well as Eq. (14) and (15) which are

$$x_{Tn}^{(iv)}(z,t) + \frac{1}{a_{Tow}^2}\,\ddot{x}_{Tn}(z,t) \;= 0\,, \qquad for\; L_{Plat} \le z \le L \tag{31}$$

$$x_{MAn}^{(iv)}(z,t) + \frac{1}{a_{MA}^2}\,\ddot{x}_{MAn}(z,t) \;= 0\,, \qquad for\; d < z \le L_{Plat} \tag{32}$$

$$x_{MUn}^{(iv)}(z,t) + \frac{1}{a_{MU}^2}\,\ddot{x}_{MUn}(z,t) \;= 0, \qquad for\; 0 < z \le d \tag{33}$$

It should be noted that the subscript n in quantity indicates that it belongs to the n^{th} natural mode. So, $x_{Tn}(z,t)$, $x_{MAn}(z,t)$, and $x_{MUn}(z,t)$ are the natural mode shapes of the tower, monopile above water and monopile underwater, respectively. The solution for the above equations is proposed in the form of

$$x_{Tn}(z,t) = X_{Tn}(z)T_{Tn}(t)\,, \qquad for\; L_{Plat} \le z \le L \tag{34}$$

$$x_{MAn}(z,t) = X_{MAn}(z)T_{MAn}(t)\,, \qquad for\; d < z \le L_{Plat} \tag{35}$$

$$x_{MUn}(z,t) = X_{MUn}(z)T_{MUn}(t), \qquad for\; 0 < z \le d \tag{36}$$

Substituting the Eqs. (34) to (36) into Eqs. (31) to (33) will yield

$$X_{Tn}^{(iv)}(z)T_{Tn}(t) + \frac{1}{a_{Tow}^2}\,X_{Tn}(z)\ddot{T}_{Tn}(t) \;= 0, \qquad for\; L_{Plat} \le z \le L \tag{37}$$

$$X_{MAn}^{(iv)}(z)T_{MAn}(t) + \frac{1}{a_{MA}^2}\,X_{MAn}(z)\ddot{T}_{MAn}(t) \;= 0, \qquad for\; d < z \le L_{Plat} \tag{38}$$

$$X_{MUn}^{(iv)}(z)T_{MUn}(t) + \frac{1}{a_{MU}^2}\,X_{MUn}(z)\ddot{T}_{MUn}(t) \;= 0, \qquad for\; 0 < z \le d \tag{39}$$

After some algebraic manipulations, they are transformed to

Journal of Offshore Mechanics and Arctic Engineering. Received April 22, 2022;
Accepted manuscript posted August 22, 2022. doi:10.1115/1.4055402

$$\frac{X_{Tn}^{(iv)}(z)}{X_{Tn}(z)} = \beta_{Tn}^4 = -\frac{1}{a_{Tow}^2}\frac{\ddot{T}_{Tn}(t)}{T_{Tn}(t)}, \qquad for\ L_{Plat} \le z \le L \tag{40}$$

$$\frac{X_{MAn}^{(iv)}(z)}{X_{MAn}(z)} = \beta_{MAn}^4 = -\frac{1}{a_{MA}^2}\frac{\ddot{T}_{MAn}(t)}{T_{MAn}(t)}, \qquad for\ d < z \le L_{Plat} \tag{41}$$

$$\frac{X_{MUn}^{(iv)}(z)}{X_{MUn}(z)} = \beta_{MUn}^4 = -\frac{1}{a_{MU}^2}\frac{\ddot{T}_{MUn}(t)}{T_{MUn}(t)}, \qquad for\ 0 < z \le d \tag{42}$$

Where β_{Tn}, β_{MAn} and β_{MUn} are the wavenumbers for the tower and monopile above water and underwater, respectively. Eqs. (40), (41), and (42) can be separated to form the following equations

$$X_{Tn}^{iv}(z) - \beta_{Tn}^4 X_{Tn}(z) = 0, \qquad for\ L_{Plat} \le z \le L \tag{43}$$

$$X_{MAn}^{iv}(z) - \beta_{MAn}^4 X_{MAn}(z) = 0, \qquad for\ d < z \le L_{Plat} \tag{44}$$

$$X_{MUn}^{iv}(z) - \beta_{MUn}^4 X_{MUn}(z) = 0, \qquad for\ 0 < z \le d \tag{45}$$

And

$$\ddot{T}_{Tn}(t) + a_{Tow}^2\,\beta_{Tn}^4\,T_{Tn}(t) = 0, \qquad for\ L_{Plat} \le z \le L \tag{46}$$

$$\ddot{T}_{MUn}(t) + a_{MU}^2\,\beta_{MUn}^4\,T_{MUn}(t) = 0, \qquad for\ d < z \le L_{Plat} \tag{47}$$

$$\ddot{T}_{MAn}(t) + a_{MA}^2\,\beta_{MAn}^4\,T_{MAn}(t) = 0, \qquad for\ 0 < z \le d \tag{48}$$

In the above six equations, the temporal and spatial variables are separated. Therefore, they can be solved independently. Since every section of a continuous system should vibrate with the same natural frequency in each mode shape, so $T_{Tn} = T_{MAn}(t) = T_{MUn}(t)$. By comparing the two Eqs. (46) and (47), one can conclude that $a_{\mathrm{Tow}}^2\,\beta_{Tn}^4 = a_{\mathrm{MU}}^2\,\beta_{MUn}^4 = a_{\mathrm{MA}}^2\,\beta_{MAn}^4$ because $T_{Tn} = T_{MAn}(t) = T_{MUn}(t)$. Therefore,

$$\ddot{T}_n(t) + \omega_n^2\,T_n(t) = 0, \qquad for\ 0 \le z \le L \tag{49}$$

Where

$$\omega_n^2 = a_{Tow}^2\,\beta_{Tn}^4 = a_{MU}^2\,\beta_{MUn}^4 = a_{MA}^2\,\beta_{MAn}^4 \tag{50}$$

Since T is a periodic function, it will oscillate with the cyclic frequency of ω_n which is a natural frequency of the system.

The solution of the motion Eqs. (34), (35), and (36) can be imposed into the boundary conditions defined by Eqs. (18) to (29) to yield the boundary conditions independent from the time variable. They are

$$X'''_{MUn}(0) + \alpha_1 X_{MUn}(0) + \alpha_2 X'_{MUn}(0) = 0, \qquad \alpha_1 = \frac{K_L}{EI_{Mon}}, \alpha_2 = \frac{K_{LR}}{EI_{Mon}} \tag{51}$$

$$X''_{MUn}(0) - \alpha_2 X_{MUn}(0) - \alpha_3 X'_{MUn}(0) = 0, \qquad \alpha_3 = \frac{K_R}{EI_{Mon}} \tag{52}$$

$$\begin{aligned} X_{MUn}(d) - X_{MAn}(d) &= 0 \\ X'_{MUn}(d) - X'_{MAn}(d) &= 0 \\ X''_{MUn}(d) - X''_{MAn}(d) &= 0 \\ X'''_{MUn}(d) - X'''_{MAn}(d) &= 0 \end{aligned} \tag{53}$$

$$\begin{aligned} X_{MAn}(L_{Plat}) - X_{Tn}(L_{Plat}) &= 0 \\ X'_{MAn}(L_{Plat}) - X'_{Tn}(L_{Plat}) &= 0 \\ X''_{MAn}(L_{Plat}) - \alpha_4 X''_{Tn}(L_{Plat}) &= 0 \\ X'''_{MAn}(L_{Plat}) - \alpha_4 X'''_{Tn}(L_{Plat}) &= 0 \end{aligned}, \qquad \alpha_4 = \frac{EI_{Tow}}{EI_{Mon}} \tag{54}$$

$$X''_{Tn}(L) - \alpha_5 \omega_n^2 X'_{Tn}(L) = 0, \qquad \alpha_5 = \frac{J_p}{EI_{Tow}} \tag{55}$$

$$X'''_{Tn}(L) + \alpha_6 \omega_n^2 X_{Tn}(L) = 0, \qquad \alpha_6 = \frac{M_n}{EI_{Tow}} \tag{56}$$

Where α_i , $i = 1 \ldots 6$ are the solution variables introduced to implement the soil-structure interactions, nacelle-blades mechanical properties, and the systems mechanical properties at sea level.

The solution for Eqs. (43), (44) and (45) are in the form of

$$X_{Tn}(z) = T_1 \cos(\beta_{Tn} z) + T_2 \cosh(\beta_{Tn} z) + T_3 \sin(\beta_{Tn} z) + T_4 \sinh(\beta_{Tn} z) \tag{57}$$

$$X_{MAn}(z) = A_1 \cos(\beta_{MAn} z) + A_2 \cosh(\beta_{MAn} z) + A_3 \sin(\beta_{MAn} z) + A_4 \sinh(\beta_{MAn} z) \tag{58}$$

$$X_{MUn}(z) = U_1 \cos(\beta_{MUn} z) + U_2 \cosh(\beta_{MUn} z) + U_3 \sin(\beta_{MUn} z) + U_4 \sinh(\beta_{MUn} z) \tag{59}$$

where T_i, A_i, and U_i are the constant coefficients for each natural mode shape. Substituting the proposed solutions expressed by Eqs. (57), (58), and (59) into the 12 boundary conditions represented by Eqs. (51) to (56) will yield a system of 12 linear equations. In matrix form, they can be represented as

$$\boldsymbol{P} \times \boldsymbol{D} = 0, \qquad \boldsymbol{D} = \{U_1\ U_2\ U_3\ U_4\ A_1\ A_2\ A_3\ A_4\ T_1\ T_2\ T_3\ T_4\}^T \tag{60}$$

Journal of Offshore Mechanics and Arctic Engineering. Received April 22, 2022;
Accepted manuscript posted August 22, 2022. doi:10.1115/1.4055402

Where **P** is the matrix containing trigonometrical and hyper trigonometrical functions and **D** is the constant coefficients vector. The concept of natural modes oscillation is that the oscillation should be independent of the constant coefficients in Eqs. (57) to (59). Therefore, the determinant of matrix **P** should be zero to yield a singular matrix. In matrix **P**, there are three variables β_{Tn}, β_{MAn} , β_{MUn} , and the singularity condition of matrix **P**. Two more conditions are needed to find them with one equation. As mentioned earlier, the cyclic frequency of the system is unique so recalling the definitions of the wavenumber from Eq. (50) and rewriting them yields

$$\beta_{MAn} = \gamma_{AT}\beta_{Tn}, \qquad \gamma_{AT} = \sqrt[4]{\alpha_4 \frac{m_{Mon}}{m_{Tow}}} \tag{61}$$

$$\beta_{MUn} = \gamma_{UT}\beta_{Tn}, \qquad \gamma_{UT} = \sqrt[4]{\alpha_4 \left(\frac{m_{Mon} + \rho_w C_A A_{Mon}}{m_{Tow}}\right)} \tag{62}$$

where γ_{UT} and γ_{AT} are defined to introduce the effect of added mass as well as the rigidity changes at sea level and platform level to the natural mode shapes, respectively. To find the coefficient matrix **D** for each natural mode, Eq. (60) should be solved by substituting the wavenumbers obtained from the singularity of matrix **P**. Finally, the natural mode shapes of the system can be found by substituting variables found for each mode in Eqs. (57), (58) and (59). By merging them, it can be represented in a single function as

$$X_n(z) = X_T(z)\, H_1(z) + X_{MA}(z) H_2(z) + X_{MU}(z) H_3(z), \qquad 0 \le z \le L \tag{63}$$

3.2. The solution for an external load

The solution of an equation of motion in the form of

$$x^{(iv)}(z,t) + \mathrm{A}(z)\, \ddot{x}(z,t) \; = \frac{1}{EI_{Mon}} H_3(z) Q(z,t) \tag{64}$$

can be obtained by using the expansion theorem to represent the motion of the tower in the form of

$$\mathrm{x}(z,t) = \sum_{n=1}^{\infty} X_n(z) T_n(t) \tag{65}$$

where the $X_n(z)$ is the natural mode of the system which satisfy

$$X_n^{(iv)} - \omega_n^2 A(z) X_n(z) = 0 \tag{66}$$

The above equation is obtained by substituting Eqs (50) into (43) and (44) and merging them by using Eq. (9). Substituting Eq. (65) into Eq. (64) yields

Journal of Offshore Mechanics and Arctic Engineering. Received April 22, 2022;
Accepted manuscript posted August 22, 2022. doi:10.1115/1.4055402

$$\sum_{n=1}^{\infty} X_n^{(iv)}(z)T_n(t) + A(z)\sum_{n=1}^{\infty} X_n(z)\ddot{T}_n(t) = \frac{1}{EI_{Mon}} H_3(z)\mathrm{Q}(\mathrm{z},\mathrm{t}) \quad (67)$$

Multiplying both sides by $X_m(z)$ and integrating over the length of the tower, it yields

$$\begin{aligned}\sum_{n=1}^{\infty} T_n(t) \int_0^L X_m(z)X_n^{(iv)}(z)\,dz + \sum_{n=1}^{\infty} \ddot{T}_n(t)\int_0^L A(z)X_m(z)X_n(z)dz \\ = \frac{1}{EI_{Mon}}\int_0^L H_3(z)Q(z,t)X_m(z)dz\end{aligned} \quad (68)$$

Substituting $X_n^{(iv)}$ from Eq. (66) into Eq. (68) results in

$$\sum_{n=1}^{\infty} \int_0^L A(z)X_m(z)X_n(z)\,dz \left(\ddot{T}_n(t) + \omega_n^2 T_n(t)\right) = \frac{1}{EI_{Mon}}\int_0^L H_3(z)Q(z,t)X_m(z)dz \quad (69)$$

The natural modes are orthogonal and normalized. Therefore, the above equation is simplified to

$$\ddot{T}_n(t) + \omega_n^2 T_n(t) = \frac{1}{EI_{Mon}}\int_0^L H_3(z)Q(z,t)X_m(z)dz \quad (70)$$

It should be noted that the natural modes are normalized such that

$$\int_0^L A(z)\,X_n^2(z)\,dz = 1 \quad (71)$$

By finding $T_n(t)$ from solving Eq. (70), it can be substituted into Eq. (65) to obtain the response of the tower.

3.3. Solution for the wave load

The wave load acting on the tower was introduced in section 2.1. It was shown that Eq. (8) governs the motion of the tower with the external load in the form of Eq. (13). It is a function of horizontal particle wave velocity, $u(z,t)$ which is defined based on the 2^{nd} order wave theory [72] as

$$u(z,t) = f_1\cosh(kz)\cos(\omega t) + f_2\cosh(2kz)\cos(2\omega t) \quad (72)$$

where

$$f_1 = \frac{\omega H}{2\sinh(kd)} \quad (73)$$

Journal of Offshore Mechanics and Arctic Engineering. Received April 22, 2022;
Accepted manuscript posted August 22, 2022. doi:10.1115/1.4055402

$$f_2 = \frac{3}{16}\frac{\omega k H^2}{\sinh^4(kd)} \tag{74}$$

Eq. (72) can be rewritten as

$$u(z,t) = f_2 \cosh(2kz)\,(f(z)\cos(\omega t) + \cos(2\omega t)) \tag{75}$$

where

$$f(z) = \frac{8}{3}\frac{\sinh^3(kd)}{k}\frac{\cosh(kz)}{\cosh(2kz)} \tag{76}$$

Substituting Eq. (75) into Eq. (13) yields

$$Q(z,t) = F_1(z,t) + H_t(z,t)\,F_2(z,t) \tag{77}$$

where

$$F_1(z,t) = -\rho_w C_M A \omega f_2 \cosh(2kz)\,(f(z)\sin(\omega t) + 2\sin(2\omega t)) \tag{78}$$

$$F_2(z,t) = \frac{1}{2}\rho_w C_D D f_2^2 \cosh^2(2kz)\,(f(z)\cos(\omega t) + \cos(2\omega t))^2 \tag{79}$$

$$H_t(z,t) = \begin{cases} +1, & u(z,t) > 0 \\ -1, & u(z,t) < 0 \end{cases} \tag{80}$$

Eq. (77) is the wave load based on Morison's formula rewritten from Eq. (13). $H_t(z,t)$ is a step function representing the absolute value function in his formula. To find the response of an OWT under this load, it needs Eq. (70) to be solved after substituting Eq. (77) in it. The resultant will be an ordinary nonhomogeneous 2nd differential equation. The solution to this differential equation can be found by solving Eq. (70) for $F_1(z,t)$ and $H_t(z,t)\,F_2(z,t)$ separately and adding them by using the superposition principle. Substituting $F_1(z,t)$ as $Q(z,t)$ into the right side of Eq. (70) and solving the integration with respect to the z variable analytically will lead to the trigonometrical functions depending on the temporal variable left on the right side of Eq. (70). The solution of it is pretty straightforward. So, the solution for $F_1(z,t)$ can be proposed in the form of Eq. (65) where $T_n(t)$ is found by solving Eq. (70) for $F_1(z,t)$.

However, the solution for Eq. (70) when the second term of Eq. (77), $H_t(z,t)\,F_2(z,t)$, is substituted as $Q(z,t)$ in the right side of it will be challenging. This term consists of $F_2(z,t)$ in Eq. (79) in which temporal and spatial functions are squared and $H_t(z,t)$ in Eq. (80) which is a step function depending on the sign of $u(z,t)$. To obtain a solution for Eq. (70) in this matter, it needs to work on these two parts to transfer them into the conventional form of functions with a combination of spatial functions and linear trigonometrical terms. To start, the squared term of Eq. (79) is expanded to obtain

Journal of Offshore Mechanics and Arctic Engineering. Received April 22, 2022;
Accepted manuscript posted August 22, 2022. doi:10.1115/1.4055402

$$F_2(z,t) = \frac{1}{2}\rho_w C_D D_{Mon} f_2^2 \, cosh^2(2kz)\,(f^2(z)\,cos^2(\omega t) + 2f(z)\,cos(\omega t)\,cos(2\omega t) + cos^2(2\omega t)) \tag{81}$$

By using the following trigonometrical relationships

$$cos^2(\theta) = \frac{1}{2}\,(cos(2\theta) + 1) \tag{82}$$

$$cos(\theta)\,cos(2\theta) = \frac{1}{2}(cos(\theta) + cos(3\theta)) \tag{83}$$

and substituting them into Eq. (81), it yields

$$F_2(z,t) = \frac{1}{4}\rho_w C_D D_{Mon} f_2^2 \cosh^2(2kz)\,(f^2(z) + 1 + 2f(z)\cos(\omega t) + f^2(z)\cos(2\omega t) + 2f(z)\cos(3\omega t) + \cos(4\omega t)) \tag{84}$$

which is a function in which the trigonometrical terms are linear.

The value of $H_t(z,t)$ can be determined by the sign of $u(z,t)$. Recalling $u(z,t)$ from Eq. (75) and using the trigonometric relationship in Eq. (82) yields

$$u(z,t) = f_2 \cosh(2kz)\,(2\cos^2(\omega t) + \; f(z)\cos(\omega t) - 1) \tag{85}$$

The above equation reveals that the sign of $u(z,t)$ depends on the values of $\cos(\omega t)$ and $f(z)$. To evaluate the sign of $u(z,t)$, one needs to find when and where it becomes zero. From Eq. (76), it can be found that $f(z)$ is continuously decreasing when z is increasing because the numerator is always smaller than the denominator. Also, $\cosh(kz)$ is always positive and $\sinh(kd)$ is positive as long as kd is positive. Therefore, $f(z)$ is always a positive quantity and does not influence the sign of $u(z,t)$. For this reason, the only term that governs the sign of $u(z,t)$ is $f(z)\cos(\omega t) + \cos(2\omega t)$. For $f(z) > 1$, there are two positive roots in the $[0,2\pi/\omega]$ domain. They are

$$t_1(z) = \frac{1}{\omega}\cos^{-1}\left(\frac{-f(z) + \sqrt{f^2(z) + 8}}{4}\right) \tag{86}$$

$$t_2(z) = \frac{2\pi}{\omega} - t_1(z) \tag{87}$$

Therefore,

$$H_t(z,t) = \begin{cases} +1, & 0 \le t < t_1(z) \; or \; t_2(z) < t \le \dfrac{2\pi}{\omega} \\ -1, & t_1(z) < t < t_2(z) \end{cases} \tag{88}$$

Journal of Offshore Mechanics and Arctic Engineering. Received April 22, 2022;
Accepted manuscript posted August 22, 2022. doi:10.1115/1.4055402

The above equation represents the value of $H_t(z,t)$ in the time domain of $[0,2\pi/\omega]$. For the time domain beyond it, the value of $H_t(z,t)$ can be evaluated by considering the time variable relative to a one-period time frame since $F_2(z,t)$ is a periodic function.

Therefore, Eq. (13) can be written in the form of

$$Q(z,t) = \sum_{i=1}^{2} P_{1i}(z)\sin(i\omega t) + H_t(z,t)P_2(z) + H_t(z,t)\sum_{j=1}^{4} P_{3j}(z)\cos(j\omega t) \tag{89}$$

where

$$P_{11}(z) = -\rho_w C_M A_{Mon}\, \omega\, f_2 \cosh(2kz)\, f(z) \tag{90}$$

$$P_{12}(z) = -2\rho_w C_M A_{Mon} \omega f_2 \cosh(2kz) \tag{91}$$

$$P_2(z) = 0.25\, \rho_w C_D D_{Mon} f_2^2 \cosh^2(2kz)\, (f^2(z)+1) \tag{92}$$

$$P_{31}(z) = 0.25\, \rho_w C_D D_{Mon} f_2^2 \cosh^2(2kz)\, 2f(z) \tag{93}$$

$$P_{32}(z) = 0.25\, \rho_w C_D D_{Mon} f_2^2 \cosh^2(2kz)\, f^2(z) \tag{94}$$

$$P_{33}(z) = P_{31}(z) \tag{95}$$

$$P_{34}(z) = 0.25\, \rho_w C_D D_{Mon} f_2^2 \cosh^2(2kz) \tag{96}$$

The solution for Eq. (89) can be found by using the superposition principle since the properties of the system is linear. The solution for Eq. (89) can be expanded in the natural modes as follows:

$$x(z,t) = \sum_{n=1}^{\infty} T_n(t) X_n(z) \tag{97}$$

where $T_n(t)$ satisfies

$$\ddot{T}_n(t) + \omega_n^2 T_n(t) = \sum_{i=1}^{2} v_{1ni} \sin(i\omega t) + v_{2n} + \sum_{j=1}^{4} v_{3nj} \cos(j\omega t) \tag{98}$$

$$v_{1\mathrm{n}i} = \frac{1}{EI_{Mon}} \int_0^d P_{1i}(z) X_n(z) dz \tag{99}$$

$$v_{2\mathrm{n}} = \frac{1}{EI_{Mon}} \int_0^d H_t(z,t) P_2(z) X_n(z) dz \tag{100}$$

$$v_{3\mathrm{nj}} = \frac{1}{EI_{Mon}} \int_0^d H_t(z,t) P_{3\mathrm{j}}(z) X_n(z) dz \tag{101}$$

Journal of Offshore Mechanics and Arctic Engineering. Received April 22, 2022;
Accepted manuscript posted August 22, 2022. doi:10.1115/1.4055402

Solving Eq. (98) is possible by using the superposition principle in three parts namely $T_{1n}(t)$, $T_{2n}(t)$, and $T_{3n}(t)$ where

$$\ddot{T}_{1n}(t) + \omega_n^2 T_{1n}(t) = \sum_{i=1}^{2} v_{1ni} \sin(i\omega t) \tag{102}$$

$$\ddot{T}_{2n}(t) + \omega_n^2 T_{2n}(t) = v_{2n} \tag{103}$$

$$\ddot{T}_{3n}(t) + \omega_n^2 T_{3n}(t) = \sum_{j=1}^{4} v_{3nj} \cos(j\omega t) \tag{104}$$

Therefore,

$$T_n(t) = T_{1n}(t) + T_{2n}(t) + T_{3n}(t) \tag{105}$$

For Eq. (100), substituting into Eq. (103) results in

$$\ddot{T}_{2n}(t) + \omega_n^2 T_{2n}(t) = \frac{1}{EI_{Mon}} \int_0^d H_t(z,t) P_2(z) X_n(z) dz \tag{106}$$

The solution for the above equation can be represented as

$$T_{2n}(t) = \frac{1}{\omega_n} \frac{1}{EI_{Mon}} \int_0^t \int_0^d H_t(z,\tau) P_2(z) X_n(z) \sin\big(\omega_n(t-\tau)\big)\, dz\, d\tau \tag{107}$$

In the above equation, the function $H_t(z,t)$ poses challenges in solving the integration analytically. To solve the double integration in the above equation, it requires the removal $H_t(z,t)$ from inside the integrations to have a conventional double integration. As defined in Eq. (88), $H_t(z,t)$ governs the sign of v_{2n}. It can be either positive or negative, depending on which time frame it is evaluated. $H_t(z,t)$ is positive in the time frame of $[0, t_1(z)]$, negative in the time frame of $[t_1(z), t_2(z)]$, positive in the time frame of $[t_2(z), t_2(z) + 2t_1(z)]$ and so on. By introducing a new integer variable, m, by which $H_t(z,t)$ is positive when m is an odd integer and an even number when it is negative. Therefore, $H_t(z,t)$ can be redefined as

$$H_t(z,t) = \begin{cases} +1, & m = 1,3,5,\ldots \\ -1, & m = 2,4,6,\ldots \end{cases} \tag{108}$$

Since $t \in [t_{e(m-1)}(z), t_{em}(z)]$, one can conclude

$$H_t(z,t) = (-1)^{m-1} \tag{109}$$

where $t_{e0}(z) = 0$, $t_{e1}(z) = t_1(z)$, $t_{e2}(z) = t_2(z)$, $t_{e3}(z) = t_2(z) + 2t_1(z)$, and so on. Substituting the above equation into Eq. (107) and reversing the integration order yields

$$\begin{aligned} T_{2n}(t) = \frac{1}{\omega_n}\frac{1}{EI_{Mon}}\int_0^d P_2(z)X_n(z)\Bigg(\int_0^{t_1(z)} \sin\big(\omega_n(t-\tau)\big)\,d\tau \\ - \int_{t_1(z)}^{t_2(z)} \sin\big(\omega_n(t-\tau)\big)\,d\tau + \int_{t_2(z)}^{t_2(z)+2t_1(z)} \sin\big(\omega_n(t-\tau)\big)\,d\tau - \cdots \\ + (-1)^{m-1}\int_{t_{e(m-1)}(z)}^{t} \sin\big(\omega_n(t-\tau)\big)\,d\tau\Bigg)\,dz \end{aligned} \tag{110}$$

383 Similarly, for Eq. (104), the solution is

$$\begin{aligned} T_{3n}(t) = \sum_{j=1}^{4}\frac{1}{\omega_n}\frac{1}{EI_{Mon}}\int_0^d P_{3\mathrm{j}}(z)X_n(z)\Bigg(\int_0^{t_1(z)} \cos(j\omega t)\sin\big(\omega_n(t-\tau)\big)\,d\tau \\ - \int_{t_1(z)}^{t_2(z)} \cos(j\omega t)\sin\big(\omega_n(t-\tau)\big)\,d\tau \\ + \int_{t_2(z)}^{t_2(z)+2t_1(z)} \cos(j\omega t)\sin\big(\omega_n(t-\tau)\big)\,d\tau - \cdots \\ + (-1)^{m-1}\int_{t_{e(m-1)}(z)}^{t} \cos(j\omega t)\sin\big(\omega_n(t-\tau)\big)\,d\tau\Bigg)\,dz \end{aligned} \tag{111}$$

384 Therefore, a method of solving the double integration in Eq. (107) is proposed by removing the
385 function $H_t(z,t)$, or better to say the staging of the integration domain, as represented in Eqs.
386 (110) and (111).

387 4. Parametric study and numerical example

388 In this section, the effect of the three solution variables, α_3, α_5, and α_6 introduced in Eqs. (52),
389 (55), and (56) representing foundation rotational stiffness, nacelle rotational mass, and nacelle
390 mass, respectively, as well as the water depth on the natural wavenumbers, and the effect of
391 added mass on the response are investigated.

392 A numerical example is represented for a reference OWT. The geometry of the system has been
393 chosen from the DTU 10 MW three-bladed OWT presented by Bak et al. [74]. The structural
394 properties are summarized in Table 2. Note that the density is considered approximately 8% more
395 than the regular steel density to take into account the mass of the components such as paint,
396 bolts, flanges and stiffeners [75]. The average tower diameter is the average of the tower
397 diameter along its height, and the average thickness is calculated from the actual tower mass [57].

398 Table 3 represents the hydrodynamic loading parameters used in this study. The coefficients are
399 chosen by the recommendations provided by DNV-RP-C205 [72].

400 The values for the coupled springs model are provided in Table 4 by the work presented by
401 Alkhoury et al. [60]. They calculated these values for the loose sand from the finite element model
402 created for their study in which the same DTU 10 MW OWT is modeled and studied.

Journal of Offshore Mechanics and Arctic Engineering. Received April 22, 2022;
Accepted manuscript posted August 22, 2022. doi:10.1115/1.4055402

For this case, the solution variables are calculated and represented in Table 5. By using the procedure described in section 3.1, the natural frequencies of the tower, $\mathrm{f_n}$, are calculated for the first six modes and represented in Table 4. The corresponding mode shapes are illustrated in Figure 2 which is to satisfy equation (71).

In Table 6, the natural frequencies are calculated for both cases of considering the added mass and without the effect of added mass. As represented, including the effect of added mass in the system decreases the natural frequencies. This effect in the 1st mode is not as significant as in higher modes. The reason can be explained by using Figure 2 where the displacement of the underwater section in 1st mode is remarkably less compared to the higher modes. Besides, the presence of the weighty nacelle-rotor assembly mass dominates the motion of the 1st mode. Therefore, the motion of the system in the higher modes is less than in the 1st mode due to the substantial inertial force at the top of the system.

4.1. Comparison with the finite element model and the degree of accuracy

To evaluate the accuracy of the results, they are compared with the study conducted by Alkhoury at el. [48,60]. They created a detailed 3D finite element (FE) model within Abaqus/Standard to compute the natural frequencies of the DTU 10 MW OWT. They used shell elements to model the tower, including the diameter variation in length and solid elements for monopile. They also fully modeled the soil inside and outside the monopile to investigate the soil structure interaction. They also performed a parametric study on the 1st natural frequency by varying the water depth and monopile's diameter and thickness. The 1st natural frequencies of the system are calculated and compared with the values they calculated for the loose sand that are represented in Table 7. Note that the values of the coupled springs used in this study are also calculated by them which are obtained from the FE model. The differences between the results obtained by the proposed model and the FE model reveal that the proposed model underestimated the 1st natural frequency for every water depth in the range between 13% to 16.8%. Alkhoury et al. [60] also compared the results of the full 3D model with the one in which the tower cross-section is constant for a water depth of 25 m. They found that simplifying modeling by considering the tower's cross-section constant reduced the 1st natural frequency by 11% for the monopile with 8.3 m in diameter and 9 cm in thickness. The findings of this paper also verify this underestimation with a 13.8% deviation. Therefore, this simplification underestimates the 1st natural frequency that requires using more complicated equations of motion to improve the accuracy of the natural frequency estimation.

4.2. Parametric study on natural wavenumbers

The effect of the water depth and solution parameters, α_3, α_5, and α_6, on the tower wavenumber, β_{Tn}, have been parametrically studied for the first 5 modes and the results have been represented in Figure 3 to Figure 6. In these figures, the tower wavenumbers are normalized to the values of β_{Tn} when $\alpha_3 = \alpha_5 = \alpha_6 = d = 0$. In this study, the ratio of water depth and tower length, d/L, varies from 0 to 1, implying $d = 0$ and $d = L$, respectively. The variation of the solution variables as well as their corresponding variation of the parameters used in the parametric study, is represented in Table 8. It should be noted that the effect of the support's lateral stiffness, K_L, and cross-coupled stiffness, K_{LR}, which are used in variables α_1 and α_2,

Journal of Offshore Mechanics and Arctic Engineering. Received April 22, 2022;
Accepted manuscript posted August 22, 2022. doi:10.1115/1.4055402

respectively, are well investigated in the literature in ref. [56]. So, their effect is not included in the parametric study. Besides, the section of the system is kept constant throughout the length for simplicity.

4.2.1. The effect of water depth

As illustrated in Figure 3, the wavenumber for the first 5 modes decreases by increasing the water depth regardless of the boundary conditions properties because of the presence of added mass to the system for the case of the properties introduced in Table 8. The value of the wavenumber in the 1st mode remains almost constant by increasing the water depth up to 0.4L and drops up to L for the case of $\alpha_6 = 0$ while the variation is almost constant for the case when $\alpha_6 = 10^{-6}$. This can be because of the domination of the heavy mass in the motion of the system in the 1st mode. The decrease of the wavenumber for the 2nd mode starts at 0.2L and decreases approximately the same amount as the 1st mode at the sea level equal to the tower length for the cases when $\alpha_6 = 0$. The initiation of the drop of wavenumber for higher modes is almost half of the previous modes. It can be concluded that the effect of shallow water compared to the tower length and consequently the added mass in the lower modes is not significant as opposed to higher modes where it drops immediately by increasing sea level. This phenomenon may be important by the fact that the free sea level varies in each wave period. Therefore, the water surface variation can significantly change higher natural wavenumbers in the shallow water proportional to the tower length for each period of wave load. However, for higher values of d/L, the lower natural modes are also influenced by sea level variation. This variation of the natural frequencies is also reported in the literature for the 1st natural modes based on the measured data in refs. [61,65].

The pattern of the variation of wavenumbers by varying the water depth shown in Figure 3 reveals a wavy-shape decrease in which the reduction rate changes in different mode numbers. It can be seen that the number of crests in this pattern is equal to the mode number. For instance, for the 2nd mode, two crests at around $d/L = 0.2$ and $d/L = 0.8$ can be seen while 5 distinguished crests are visible in the figure for mode 5. Therefore, it can be concluded that the variation of wavenumbers versus d/L is converging to a linear reduction rate.

4.2.2. The effect of support rotational stiffness, $\boldsymbol{\alpha_3}$

Figure 4 illustrates the variation of the wavenumber against the different values of α_3 in 1st and 5th modes at $d/L = 0.227$, for instance. As expected, by increasing α_3, or decreasing the support's rotational stiffness, the value of the wavenumber decreases linearly in the 1st mode and nonlinearly in the 5th mode. By increasing the rotational softness of the support the wavenumbers for all natural modes decrease. This is because the higher rotational softness provides higher rotation in the support resulting in a reduction of the wavenumbers. In the 1st mode, the effect of α_3 is more than in the 5th mode. Also, the impact of the α_3 is less in higher values of the α_5 and α_6.

4.2.3. The effect of nacelle-rotor assembly rotational moment of inertia, $\boldsymbol{\alpha_5}$

The parametric study on α_5 has been illustrated in Figure 5 for the 1st and 5th modes for two values of $\alpha_3 = \infty$ & 0.2 and $\alpha_3 = 0$ & 10^{-6} for $d/L = 0.6$ when the values of α_5 varying between 0 and

Journal of Offshore Mechanics and Arctic Engineering. Received April 22, 2022;
Accepted manuscript posted August 22, 2022. doi:10.1115/1.4055402

10^{-3}. As it can be seen in Figure 5-a, the wavenumber decreases by increasing α_5 for the 1st mode. For the 6th mode, the natural wavenumber is almost insensitive to the variation of α_5 despite a rapid decrease of natural wavenumber at small values of α_5. The decrease of wavenumber can be explained by the fact that the rotational moment of inertia at the top of the tower increases the mass momentum of the system at the top. Therefore, the moment of inertia due to the nacelle-rotor assembly causes the system to oscillate slower, yielding to the lower values of the natural wavenumbers.

4.2.4. The effect of the nacelle mass, $\boldsymbol{\alpha_6}$

Figure 6 illustrates the variation of the wavenumber against α_6 ranging from 0 to 10^{-6} for two values of $\alpha_3 = \infty$ & 0.2 and $\alpha_5 = 0$ & 10^{-3} in 1st and 5th mode when $d/L = 0.6$. A reduction can be seen in Figure 6-a for all cases of α_3 and α_5 in 1st mode. By increasing α_6, which is the increase of the top mass with respect to the tower's flexural rigidity, the motion of the tower becomes slower yielding to the smaller values of the natural wavenumbers.

The reduction effect of α_6, which is proportional to the nacelle-rotor assembly mass, can be explained by the whipping effect of the tower. The inertia of the heavy mass at the top of the tower may cause a delayed motion relative to the mid-section of the tower in the same direction. When the mid-section of the tower reaches its maximum displacement, the top section is still moving imposing extra shear force to the mid-section pushing it to move further, consequently, increasing the oscillation period, decreasing the frequency, and decreasing the wavenumber of the system, see Eq. (50). Physically speaking, the heavy mass at the top of the tower produces an inertia force in the opposite direction of the motion which slows down the motion of the tower.

In higher modes, as illustrated in Figure 6, the variation of the natural wavenumber of the system is a smooth reduction despite a rapid reduction in the small values of α_6. The reason for that can be explained by the fact that the translational acceleration at the top of the tower in higher modes is relatively smaller than that of the lower modes due to the whipping effect explained earlier. This makes higher modes less sensitive to the variation of the nacelle mass. Furthermore, this effect can also be seen in Figure 3 where the curves are gathering together by increasing the mode number implying that the effect of the boundary conditions at both sides of the system are fading out of the natural wavenumbers.

4.3. The response of the reference tower to the wave load

The wave load introduced in Eq. (89) is applied to the system and the response is evaluated by Eq. (97). The properties of Stokes's wave kinematics applied to Morison's formula are briefly represented. The proposed model's ability to deal with the difficulties posed by the drag term is explained. Besides, the effect of the added mass on the response is investigated for a certain wave load configuration. Finally, a comparison is performed between the responses obtained by the proposed solution and the numerical one.

4.3.1. The application of the wave load in the proposed solution

The inherent properties of wave load based on Morison's formula with Stokes's wave kinematics raise some difficulties in evaluating the response of the tower. Before presenting how the

Journal of Offshore Mechanics and Arctic Engineering. Received April 22, 2022;
Accepted manuscript posted August 22, 2022. doi:10.1115/1.4055402

proposed solution deals with these properties, one needs to discuss the properties of the wave load with Morison's equation introduced in Eq. (89). To this end, an ocean wave with a height of 5.1 m and a length of 132 m is chosen. This ocean wave represents a normal sea state of a water depth of 35 m in a wind speed of 26 m/s which is reported as a nonlinear ocean wave state in the ref. [76]. The properties of this ocean wave are represented in Table 9. The wave horizontal particle velocity, $u(z,t)$, introduced in Eq. (72) and the corresponding ocean wave load are drawn in Figure 7 a&b, respectively. As expected, the wave horizontal particle velocity is a periodic but non-symmetric function, which is the property of the 2nd order wave theory. The wave load is also not started from zero as shown in Figure 7 because of the presence of the cosine function in the drag term of the wave load formula.

Moreover, Figure 7-a reveals that the wave horizontal particle velocity, $u(z,t)$, does not become zero at the same time for all values of z. This is the second property of the 2nd order wave theory that causes difficulties in obtaining the response of a system loaded with it. Therefore, the situation in which $u(z,t)=0$, depends on temporal and special variables. This is shown more precisely in Figure 8 for the variation of $u(z,t)$ in the z-direction for some instant of time around the first zero value. Therefore, two functions of $t_1(z)$ and $t_2(z)$ represented by Eqs. (86) and (87) are defined to evaluate the time when $u(z,t)$ is zero. The importance of defining these two functions is to evaluate the absolute value function in the drag term of the wave load, $u(z,t)|u(z,t)|$, in Eq. (13). To compensate for the absolute value function, $H_t(z,t)$ is defined as a function $t_1(z)$ and $t_2(z)$ in Eq. (80). This poses difficulties in evaluating Eqs. (100) and (101). By defining $H_t(z,t)$ as Eq. (109) and carrying out the integration, it becomes possible to remove $H_t(z,t)$. In addition, changing the integration order by which the temporal integration is taken first in the domain as a function of $t_1(z)$ and $t_2(z)$ results in trigonometrical functions. By introducing $t_1(z)$ and $t_2(z)$ and their combinations in periods, the special outer integration can be evaluated analytically since those are functions of reversed trigonometrical functions as can be seen in Eqs. (86) and (87). Therefore, the response can be obtained as a function without any need for numerical evaluation.

The presence of $H_t(z,t)$ in the wave load is quite essential. To show this, an imaginary wave load based on Eq. (77) is defined as $F_1(z,t)+F_2(z,t)$. By drawing it together with the wave load in Eq. (77), the effect of the $H_t(z,t)$ reveals itself. Figure 9 illustrates this comparison at the sea level, z=35. It can be seen that $H_t(z,t)$ causes significant changes in the wave load when $u(z,t)$ is negative between $t_1(z)$ and $t_2(z)$. Therefore, its presence cannot be neglected in evaluating the response. However, the severity of this effect may be different in other wave configurations.

4.3.2. The response of the reference tower to the 2nd wave load

The response history of the system is illustrated in Figure 10 at different heights in which the first 5 natural modes are participating. The selected wave height and length correspond to a wave frequency of 0.1 Hz, T= 9.52 sec, which is way below the first natural frequency of the reference tower, 0.1663 Hz, represented in Table 9. As seen in Figure 10, the maximum deflection occurs at the top of the towers reaching 0.13 m. In addition, the time history deflection curve in Figure 10 reveals that the responses are a non-periodic vibration even though the loading is periodic. This can be because of the indirect presence of the term $H_t(z,t)$ in the response in Eqs. (110) and (111). The indirect presence of $H_t(z,t)$ in the response shows itself by being displayed in different time frames when the direction of the wave horizontal particle velocity changes. This triggers the transient responses at the beginning of each stage causing the response to be non-periodic. Moreover, Figure 10 shows that the natural frequencies originating from the transient response are carried by the steady-state response. This also causes the response to be non-periodic.

The deflection of the reference tower at the early stages of motion is illustrated in Figure 11. The motion starts from the rest initial condition and follows by imposing the wave load up to sea level, in this case, 35 m, causing the lower sections of the tower to move while the movement of the upper section is delayed because of the nacelle mass and tower softness. This can be referred to as the *whipping effect* when the motion of the upper sections is amplified by the motion of the lower sections of the tower. This effect can be seen clearly in the motion of the reference tower which has low stiffness or heavy nacelle mass at the top. Moreover, by looking at the deflection of the reference tower in Figure 11 for time instants from t/T=0.08 up to 0.1, T being the period of the wave which is 9.6 sec, it implies that the motion of the tower in low sections is slowing down while the upper section is still moving towards the negative deflections representing an instance for the whipping effect. It should be mentioned that the wave load at zero time is a positive value, as seen in Figure 7-b, decreasing in the early stages of the loading and reversing its direction as time passes.

4.3.3. The effect of added mass on the response

The inertia term of Morison's formula adds an extra mass to the system up to the sea level. To represent its effect on the response of the reference tower, it is evaluated by considering $C_A = 1$ and $C_A = 0$ to simulate a system with and without the presence of the added mass, respectively, and the time history responses are illustrated in Figure 12 at the nacelle level. As mentioned in section 4.1.1 and illustrated in Figure 3, the value of the system's natural wavenumbers decreases by increasing the sea level resulting from the decrease in natural frequencies based on Eq. (50). This leads the system with added mass oscillating with higher natural periods falling forward than the one without added mass, as seen in Figure 12. Furthermore, as seen in Table 6, the added mass is significantly influenced in the 2nd and higher natural frequencies in the case of the system of this study. The differences between the natural frequencies in higher modes are visible in Figure 12.

The effect of the added mass up to the sea level can also be seen in the early stages of the loading in Figure 13. The added mass increases the inertia force of the system. The higher the inertia force is, the slower the vibration results. Therefore, the system's motion with added mass included delays compared to the one without the added mass as seen in Figure 13. It is also revealing that the added mass is appended to the system up to sea level, providing lower deflection at the lower sections of the system while the upper sections have almost the same deflection. The overall interpretation from Figure 13 reveals that the effect of the added mass up to the sea level is successfully simulated by the proposed solution.

4.3.4. Comparison with numerical results

The derived formulation of the response of the system is based on the expansion in the natural modes. The accuracy of the solution depends on the number of natural modes participating in the solution. For a continuous system, an infinite number of modes is expected. The higher number

Journal of Offshore Mechanics and Arctic Engineering. Received April 22, 2022;
Accepted manuscript posted August 22, 2022. doi:10.1115/1.4055402

of modes participating in the solution, the more accurate the response obtained. It is worthwhile to mention that the Bernoulli-Euler beam theory in the form of Eq. (1) is applicable for the lower natural modes only. In higher modes, the shearing deformation and rotatory inertia significantly affect the natural frequencies [50]. Therefore, reaching higher natural modes requires the equation of motion with those effects considered. However, as far as the wave load by using Morison's formula matters, its validity requires that the ocean wavelength should be five times [72] higher than the diameter of the slender structure. This limitation causes the frequency of the ocean wave load to be lower than the system's first natural frequency. Therefore, only the first few natural modes may be enough to evaluate the tower's response.

To confirm the accuracy of the proposed solution, a numerical evaluation is performed by using the standard commercial software *Mathematica*® [77]. The partial differential numerical solver, *NDSolve*, is chosen to solve Eq. (8) by introducing the wave velocity from Eq. (72). The properties of the system chosen for the numerical evaluation are represented in Table 10.

The wave height, H, and length, λ, are selected to be 3 and 100 meters, respectively. By setting *MaxStepSize* equal to 1.4, and *AccuracyGoal* and *PrecisionGoal* to 6, *NDsolve* solves the PDE by using the Hermite method in orders of 7 and 3 in z and t variables, respectively, in the domain of $z \in [0,115]$ and $t \in [0,34]$. Besides, the first 6 natural modes of the tower with the properties and loading the same as the numerical one are selected for participating in the proposed solution results. The comparison between the response obtained by the numerical solution and the proposed one verifies the perfect agreement between the two methods, as illustrated in Figure 14.

5. Conclusions

An analytical solution for the modal analysis of offshore wind turbine strucutres has been developed. The solution includes the wave-structure interaction by appending an extra mass to the system underwater. In an effort to propose a more accurate solution based on the classical analytical methods, the flexibility of the foundation as well as the inertial forces induced by the nacelle-rotor assembly translational and rotational inertia are assigned to the boundaries of the system. Besides, the considerable cross-sectional changes at the platform level where the monopile is connected to the tower by a transition part are taken into account in the solution. Overall, a system of three partial differential equations consisting of 12 boundary conditions and 2 initial conditions has been solved using the expansion theorem.

The effect of water depth, foundation rotational flexibility, nacelle mass, and nacelle-blades rotational inertia on the system's natural wavenumber were studied parametrically for the first 5 natural modes of the system. The results reveal that:

1. The natural wavenumber decreases by increasing the water depth to the tower-length ratio, d/L, for all natural modes producing a wavy pattern based on the modal number. The effect of the foundation rotational flexibility, nacelle-blades rotational inertia, and nacelle mass on the natural wavenumber decreases by increasing the modal number for all sea level values. More importantly, the variation of the natural wavenumbers by variation of the sea level implies that the natural wavenumbers or natural frequencies of

Journal of Offshore Mechanics and Arctic Engineering. Received April 22, 2022;
Accepted manuscript posted August 22, 2022. doi:10.1115/1.4055402

the system vary during sea level variation during a period of wave load. Therefore, the system's natural frequencies can be considered a time-dependent quantity. It can be essential in the assessment of the ringing-type resonance of the system and fatigue loading.

2. The system's natural frequencies decrease by increasing the foundation rotational flexibility, mass and the rotational inertial of the nacelle-rotor assembly. This pattern has been seen at all water depths.
3. The proposed model, based on the simplification of considering the constant cross-section for the tower, underestimates the 1st natural frequency of the system between 13% to 16.8%. Reaching higher accuracy requires establishing more complicated equations of motions by accounting for the cross-sectional variation of the tower. However, the proposed method is straightforward and agile in calculating cost-efficient natural frequencies.

The solution for the undamped response of the tower under the wave load with 2nd order Stokes's wave theory based on Morison's formula has been developed as an analytical function. Two major contributions are

1. The drag term of Morison's formula, neglected by many researchers, is successfully included in finding the response of the system by defining $H_t(z,t)$ to remove the absolute value function in the drag term.
2. The comparison made between the responses of the system with and without added mass showed that the presence of added mass up to the sea level changes the shape of the response. This also can be important in fatigue evaluation of the system by providing a more realistic estimation of the stress status in the structure.

6. References

[1] Wind Europe. 2019. "The European Offshore Wind Industry - Key Trends and Statistics 2019." *Wind Europe*. Wind Europe. https://windeurope.org/intelligence-platform/product/wind-energy-in-europe-in-2019-trends-and-statistics/.

[2] Adeli, Hojjat, Kim, Hongjin. 2009. *Wavelet-Based Vibration Control of Smart Buildings and Bridges*. Florida: CRC Press, Taylor & Francis, Boca Raton.

[3] Kim, Hongjin, and Hojjat Adeli. 2004. "Hybrid Feedback-Least Mean Square Algorithm for Structural Control." *Journal of Structural Engineering* 130 (1). https://doi.org/10.1061/(asce)0733-9445(2004)130:1(120).

[4] Adeli, H., and A. Saleh. 1997. "Optimal Control of Adaptive/Smart Bridge Structures." *Journal of Structural Engineering* 123 (2): 218–26. https://doi.org/10.1061/(asce)0733-9445(1997)123:2(218).

[5] Saleh, A., and H. Adeli. 1994. "Parallel Algorithms for Integrated Structural/Control Optimization." *Journal of Aerospace Engineering* 7 (3). https://doi.org/10.1061/(asce)0893-1321(1994)7:3(297).

[6] Saleh, A., and H. Adeli. 1996. "Parallel Eigenvalue Algorithms for Large-Scale Control-Optimization Problems." *Journal of Aerospace Engineering* 9 (3): 70–79.

Journal of Offshore Mechanics and Arctic Engineering. Received April 22, 2022;
Accepted manuscript posted August 22, 2022. doi:10.1115/1.4055402

https://doi.org/10.1061/(asce)0893-1321(1996)9:3(70).

[7] Saleh, A., and H. Adeli. 1997. "Robust Parallel Algorithms for Solution of Riccati Equation." *Journal of* Aerospace *Engineering* 10 (3): 126–33. https://doi.org/10.1061/(asce)0893-1321(1997)10:3(126).

[8] El-Khoury, Omar, and Hojjat Adeli. 2013. "Recent Advances on Vibration Control of Structures Under Dynamic Loading." *Archives of Computational Methods in Engineering* 20 (4): 353–60. https://doi.org/10.1007/s11831-013-9088-2.

[9] Gutierrez Soto, Mariantonieta, and Hojjat Adeli. 2017. "Recent Advances in Control Algorithms for Smart Structures and Machines." *Expert Systems* 34 (2). https://doi.org/10.1111/exsy.12205.

[10] Ghaedi, Khaled, Zainah Ibrahim, Hojjat Adeli, and Ahad Javanmardi. 2017. "Invited Review: Recent Developments in Vibration Control of Building and Bridge Structures." *Journal of Vibroengineering*. https://doi.org/10.21595/jve.2017.18900.

[11] Jiang, Xiaomo, and Hojjat Adeli. 2008. "Neuro-Genetic Algorithm for Non-Linear Active Control of Structures." *INTERNATIONAL JOURNAL FOR NUMERICAL METHODS IN ENGINEERING Int. J. Numer. Meth. Engng* 75: 770–86. https://doi.org/10.1002/nme.2274.

[12] Jiang, Xiaomo, and Hojjat Adeli. 2008. "Dynamic Fuzzy Wavelet Neuroemulator for Non-Linear Control of Irregular Building Structures." *INTERNATIONAL JOURNAL FOR NUMERICAL METHODS IN ENGINEERING Int. J. Numer. Meth. Engng* 74: 1045–66. https://doi.org/10.1002/nme.2195.

[13] Li, Zhijun, and Hojjat Adeli. 2016. "New Discrete-Time Robust H2/H∞ Algorithm for Vibration Control of Smart Structures Using Linear Matrix Inequalities." *Engineering Applications of Artificial Intelligence* 55: 47–57. https://doi.org/10.1016/j.engappai.2016.05.008.

[14] Gutierrez Soto, Mariantonieta, and Hojjat Adeli. 2017. "Many-Objective Control Optimization of High-Rise Building Structures Using Replicator Dynamics and Neural Dynamics Model." *Structural and Multidisciplinary Optimization* 56 (6): 1521–37. https://doi.org/10.1007/s00158-017-1835-9.

[15] Soto, Gutierrez, and Hojjat Adeli. 2017. "Multi-Agent Replicator Controller for Sustainable Vibration Control of Smart Structures Mariantonieta." *Journal of Vibroengineering* 19 (6): 4300–4322. https://doi.org/10.21595/jve.2017.18924.

[16] Gutierrez Soto, Mariantonieta, and Hojjat Adeli. 2018. "Vibration Control of Smart Base-Isolated Irregular Buildings Using Neural Dynamic Optimization Model and Replicator Dynamics." Engineering *Structures* 156 (February): 322–36. https://doi.org/10.1016/j.engstruct.2017.09.037.

[17] Li, Zhijun, and Hojjat Adeli. 2018. "Control Methodologies for Vibration Control of Smart Civil and Mechanical Structures." *Expert Systems* 35 (6). https://doi.org/10.1111/exsy.12354.

[18] Gutierrez Soto, Mariantonieta, and Hojjat Adeli. 2019. "Semi-Active Vibration Control of Smart Isolated Highway Bridge Structures Using Replicator Dynamics." *Engineering Structures* 186: 536–52. https://doi.org/10.1016/j.engstruct.2019.02.031.

[19] Javadinasab Hormozabad, Sajad, and Mariantonieta Gutierrez Soto. 2021. "Real-Time

Journal of Offshore Mechanics and Arctic Engineering. Received April 22, 2022;
Accepted manuscript posted August 22, 2022. doi:10.1115/1.4055402

Damage Identification of Discrete Structures via Neural Networks Subjected to Dynamic Loading." In , 87. https://doi.org/10.1117/12.2582482.

[20] Azimi, Mohsen, Armin Dadras Eslamlou, and Gokhan Pekcan. 2020. "Data-Driven Structural Health Monitoring and Damage Detection through Deep Learning: State-Ofthe- Art Review." *Sensors (Switzerland)* 20 (10). https://doi.org/10.3390/s20102778.

[21] Ngeljaratan, Luna, Mohamed A. Moustafa, and Gokhan Pekcan. 2021. "A Compressive Sensing Method for Processing and Improving Vision-Based Target-Tracking Signals for Structural Health Monitoring." *Computer-Aided Civil and Infrastructure Engineering* 36 (9): 1203–23. https://doi.org/10.1111/mice.12653.

[22] Long, James, and Oral Büyüköztürk. 2020. "Collaborative Duty Cycling Strategies in Energy Harvesting Sensor Networks." *Computer-Aided Civil and Infrastructure Engineering* 35 (6). https://doi.org/10.1111/mice.12522.

[23] Sajedi, Seyedomid, and Xiao Liang. 2021. "Dual Bayesian Inference for Risk-Informed Vibration-Based Damage Diagnosis." *Computer-Aided Civil and Infrastructure Engineering* 36 (9): 1168–84. https://doi.org/10.1111/mice.12642.

[24] Sajedi, Seyed Omid, and Xiao Liang. 2021. "Uncertainty-Assisted Deep Vision Structural Health Monitoring." *Computer-Aided Civil and Infrastructure Engineering* 36 (2): 126–42. https://doi.org/10.1111/mice.12580.

[25] Huang, C. S., Q. T. Le, W. C. Su, and C. H. Chen. 2020. "Wavelet-Based Approach of Time Series Model for Modal Identification of a Bridge with Incomplete Input." *Computer-Aided Civil and Infrastructure Engineering* 35 (9). https://doi.org/10.1111/mice.12539.

[26] Gil-Gala, Francisco J, Carlos Mencía, María R Sierra, and Ramiro Varela. 2021. "Learning Ensembles of Priority Rules for Online Scheduling by Hybrid Evolutionary Algorithms." *Integrated Computer-Aided Engineering* 28: 65–80. https://doi.org/10.3233/ICA-200634.

[27] Sørensen, René Arendt, Michael Nielsen, and Henrik Karstoft. 2020. "Routing in Congested Baggage Handling Systems Using Deep Reinforcement Learning." *Integrated Computer-Aided Engineering* 27 (2): 139–52. https://doi.org/10.3233/ICA-190613.

[28] Ni, Fu Tao, Jian Zhang, and Mohammad N. Noori. 2020. "Deep Learning for Data Anomaly Detection and Data Compression of a Long-Span Suspension Bridge." *Computer-Aided Civil and Infrastructure Engineering* 35 (7). https://doi.org/10.1111/mice.12528.

[29] Ren, Qiubing, Mingchao Li, Heng Li, Lingguang Song, Wen Si, and Han Liu. 2021. "A Robust Prediction Model for Displacement of Concrete Dams Subjected to Irregular Water-Level Fluctuations." *Computer-Aided Civil and Infrastructure Engineering* 36 (5). https://doi.org/10.1111/mice.12654.

[30] Ghofrani, Faeze, Abhishek Pathak, Reza Mohammadi, Amjad Aref, and Qing He. 2020. "Predicting Rail Defect Frequency: An Integrated Approach Using Fatigue Modeling and Data Analytics." *Computer-Aided Civil and Infrastructure Engineering* 35 (2). https://doi.org/10.1111/mice.12453.

[31] Tong, Zheng, Dongdong Yuan, Jie Gao, and Zhenjun Wang. 2020. "Pavement Defect Detection with Fully Convolutional Network and an Uncertainty Framework." *Computer-Aided Civil and Infrastructure Engineering* 35 (8): 832–49.

Journal of Offshore Mechanics and Arctic Engineering. Received April 22, 2022;
Accepted manuscript posted August 22, 2022. doi:10.1115/1.4055402

https://doi.org/10.1111/mice.12533.

[32] Kalenjuk, Slaven, Werner Lienhart, and Matthias J. Rebhan. 2021. "Processing of Mobile Laser Scanning Data for Large-Scale Deformation Monitoring of Anchored Retaining Structures along Highways." *Computer-Aided Civil and Infrastructure Engineering* 36 (6). https://doi.org/10.1111/mice.12656.

[33] Zhu, Mengqi, Hehua Zhu, Feng Guo, Xueqin Chen, and J. Woody Ju. 2021. "Tunnel Condition Assessment via Cloud Model-Based Random Forests and Self-Training Approach." *Computer-Aided Civil and Infrastructure Engineering* 36 (2). https://doi.org/10.1111/mice.12601.

[34] Amezquita-Sanchez, Juan P., Hyo Seon Park, and Hojjat Adeli. 2017. "A Novel Methodology for Modal Parameters Identification of Large Smart Structures Using MUSIC, Empirical Wavelet Transform, and Hilbert Transform." *Engineering Structures* 147 (September): 148–59.

[35] Pavlou, Dimitrios. 2022. "A Deterministic Algorithm for Nonlinear, Fatigue-Based Structural Health Monitoring." *Computer-Aided Civil and Infrastructure Engineering* 37 (7). https://doi.org/10.1111/mice.12783.

[36] Bjørheim, Fredrik, Sudath C. Siriwardane, and Dimitrios Pavlou. 2022. "A Review of Fatigue Damage Detection and Measurement Techniques." *International Journal of Fatigue* 154 (January): 106556. https://doi.org/10.1016/J.IJFATIGUE.2021.106556.

[37] Bjørheim, Fredrik, Dimitrios G Pavlou, | Sudath, and C Siriwardane. 2022. "Nonlinear Fatigue Life Prediction Model Based on the Theory of the S-N Fatigue Damage Envelope." https://doi.org/10.1111/ffe.13680.

[38] Luan, M, P Qu, D S Jeng, Y Guo, and Q Yang. 2008. "Dynamic Response of a Porous Seabed–Pipeline Interaction under Wave Loading: Soil–Pipeline Contact Effects and Inertial Effects." *Computers and Geotechnics* 35 (2): 173–86. https://doi.org/10.1016/j.compgeo.2007.05.004.

[39] Li, Xiao-Jun, Fu-Ping Gao, Bing Yang, and Jun Zang. 2011. "Wave-Induced Pore Pressure Responses And Soil Liquefaction Around Pile Foundation." *International Journal of Offshore and Polar Engineering* 21 (03).

[40] Chang, Kun Tan, and Dong Sheng Jeng. 2014. "Numerical Study for Wave-Induced Seabed Response around Offshore Wind Turbine Foundation in Donghai Offshore Wind Farm, Shanghai, China." *Ocean Engineering* 85: 32–43. https://doi.org/10.1016/j.oceaneng.2014.04.020.

[41] Chen, L F, J Zang, A J Hillis, G. C.J. Morgan, and A R Plummer. 2014. "Numerical Investigation of Wave-Structure Interaction Using OpenFOAM." *Ocean Engineering* 88: 91–109. https://doi.org/10.1016/j.oceaneng.2014.06.003.

[42] Sui, Titi, Chi Zhang, Yakun Guo, Jinhai Zheng, Dongsheng Jeng, Jisheng Zhang, and Wei Zhang. 2015. "Three-Dimensional Numerical Model for Wave-Induced Seabed Response around Mono-Pile." *Ships and Offshore Structures* 11 (6): 667–78. https://doi.org/10.1080/17445302.2015.1051312.

[43] Zhang, Chi, Qingyang Zhang, Zaitian Wu, Jisheng Zhang, Titi Sui, and Yuncheng Wen. 2015.

Journal of Offshore Mechanics and Arctic Engineering. Received April 22, 2022;
Accepted manuscript posted August 22, 2022. doi:10.1115/1.4055402

“Numerical Study on Effects of the Embedded Monopile Foundation on Local Wave-Induced Porous Seabed Response.” *Mathematical Problems in Engineering* 2015: 1–13. https://doi.org/10.1155/2015/184621.

[44] Lin, Zaibin, Dubravka Pokrajac, Yakun Guo, Dong-sheng Jeng, Tian Tang, Nick Rey, Jinhai Zheng, and Jisheng Zhang. 2017. “Investigation of Nonlinear Wave-Induced Seabed Response around Mono-Pile Foundation.” *Coastal Engineering* 121: 197–211. https://doi.org/10.1016/j.coastaleng.2017.01.002.

[45] Bazeos, N., G. D. Hatzigeorgiou, I. D. Hondros, H. Karamaneas, D. L. Karabalis, and D. E. Beskos. 2002. “Static, Seismic and Stability Analyses of a Prototype Wind Turbine Steel Tower.” *Engineering Structures* 24 (8): 1015–25. https://doi.org/10.1016/S0141-0296(02)00021-4.

[46] Murtagh, P J, B Basu, and B M Broderick. 2005. “Along-Wind Response of a Wind Turbine Tower with Blade Coupling Subjected to Rotationally Sampled Wind Loading.” *Engineering Structures* 27 (8): 1209–19. https://doi.org/10.1016/j.engstruct.2005.03.004.

[47] Lavassas, I, G Nikolaidis, P Zervas, E Efthimiou, I N Doudoumis, and C C Baniotopoulos. 2003. “Analysis and Design of the Prototype of a Steel 1-MW Wind Turbine Tower.” *Engineering Structures* 25 (8): 1097–1106. https://doi.org/10.1016/s0141-0296(03)00059-2.

[48] Alkhoury, Philip, Abdul-Hamid Soubra, Valentine Rey, and Mourad Aït-Ahmed. 2022. “Dynamic Analysis of a Monopile-Supported Offshore Wind Turbine Considering the Soil-Foundation-Structure Interaction.” *Soil Dynamics and Earthquake Engineering* 158 (July): 107281. https://doi.org/10.1016/J.SOILDYN.2022.107281.

[49] Graff, K F. 2012. *Wave Motion in Elastic Solids*. Dover Publications.

[50] Meirovitch, L. 1967. *Analytical Methods in Vibrations*. Macmillan. https://books.google.no/books?id=sf1QAAAAMAAJ.

[51] Pavlou, Dimitrios G. 2021. “Soil–Structure–Wave Interaction of Gravity-Based Offshore Wind Turbines: An Analytical Model.” *Journal of Offshore Mechanics and Arctic Engineering* 143 (3). https://doi.org/10.1115/1.4048997.

[52] Wang, Jianhong, Datong Qin, and Teik C Lim. 2010. “Dynamic Analysis of Horizontal Axis Wind Turbine by Thin-Walled Beam Theory.” *Journal of Sound and Vibration* 329 (17): 3565–86. https://doi.org/10.1016/j.jsv.2010.03.011.

[53] Adeli, Hojjat, and Asim Karim. 1997. “Neural Network Model for Optimization of Cold-Formed Steel Beams.” *Journal of Structural Engineering* 123 (11). https://doi.org/10.1061/(asce)0733-9445(1997)123:11(1535).

[54] Karim, Asim, and Hojjat Adeli. 1999. “Global Optimum Design of Cold-Formed Steel Hat-Shape Beams.” *Thin-Walled Structures* 35 (4). https://doi.org/10.1016/s0263-8231(99)00033-6.

[55] Tashakori, A., and H. Adeli. 2002. “Optimum Design of Cold-Formed Steel Space Structures Using Neural Dynamics Model.” *Journal of Constructional Steel Research* 58 (12): 1545–66. https://doi.org/10.1016/S0143-974X(01)00105-5.

[56] Arany, L, S Bhattacharya, S Adhikari, S J Hogan, and J H G Macdonald. 2015. “An Analytical

Model to Predict the Natural Frequency of Offshore Wind Turbines on Three-Spring Flexible Foundations Using Two Different Beam Models." *Soil Dynamics and Earthquake Engineering* 74: 40–45. https://doi.org/10.1016/j.soildyn.2015.03.007.

[57] Arany, Laszlo, S Bhattacharya, John H.G. Macdonald, and S John Hogan. 2016. "Closed Form Solution of Eigen Frequency of Monopile Supported Offshore Wind Turbines in Deeper Waters Incorporating Stiffness of Substructure and SSI." *Soil Dynamics and Earthquake Engineering* 83: 18–32. https://doi.org/10.1016/j.soildyn.2015.12.011.

[58] Amar Bouzid, Djillali, Subhamoy Bhattacharya, and Lalahoum Otsmane. 2018. "Assessment of Natural Frequency of Installed Offshore Wind Turbines Using Nonlinear Finite Element Model Considering Soil-Monopile Interaction." *Journal of Rock Mechanics and Geotechnical Engineering* 10 (2): 333–46. https://doi.org/10.1016/j.jrmge.2017.11.010.

[59] Adeli, Hojjat, James M. Gere, and William Weaver. 1978. "ALGORITHMS FOR NONLINEAR STRUCTURAL DYNAMICS." *ASCE J Struct Div* 104 (2). https://doi.org/10.1061/jsdeag.0004855.

[60] Alkhoury, Philip, Abdul Hamid Soubra, Valentine Rey, and Mourad Aït-Ahmed. 2021. "A Full Three-Dimensional Model for the Estimation of the Natural Frequencies of an Offshore Wind Turbine in Sand." *Wind Energy* 24 (7): 699–719. https://doi.org/10.1002/we.2598.

[61] Damgaard, M, L B Ibsen, L. V. Andersen, and J. K.F. Andersen. 2013. "Cross-Wind Modal Properties of Offshore Wind Turbines Identified by Full Scale Testing." *Journal of Wind Engineering and Industrial Aerodynamics* 116: 94–108. https://doi.org/10.1016/j.jweia.2013.03.003.

[62] Prendergast, L J, K Gavin, and P Doherty. 2015. "An Investigation into the Effect of Scour on the Natural Frequency of an Offshore Wind Turbine." *Ocean Engineering* 101: 1–11. https://doi.org/10.1016/j.oceaneng.2015.04.017.

[63] Prendergast, L J, C Reale, and K Gavin. 2018. "Probabilistic Examination of the Change in Eigenfrequencies of an Offshore Wind Turbine under Progressive Scour Incorporating Soil Spatial Variability." *Marine Structures* 57: 87–104. https://doi.org/10.1016/j.marstruc.2017.09.009.

[64] Dong, Xiaofeng, Jijian Lian, Haijun Wang, Tongshun Yu, and Yue Zhao. 2018. "Structural Vibration Monitoring and Operational Modal Analysis of Offshore Wind Turbine Structure." *Ocean Engineering* 150: 280–97. https://doi.org/10.1016/j.oceaneng.2017.12.052.

[65] Norén-Cosgriff, Karin, and Amir M Kaynia. 2021. "Estimation of Natural Frequencies and Damping Using Dynamic Field Data from an Offshore Wind Turbine." *Marine Structures* 76. https://doi.org/10.1016/j.marstruc.2020.102915.

[66] Natarajan, Anand. 2014. "Influence of Second-Order Random Wave Kinematics on the Design Loads of Offshore Wind Turbine Support Structures." *Renewable Energy* 68: 829–41.

[67] Wang, Yingguang. 2020. "Bottom Effects on the Tower Base Shear Forces and Bending Moments of a Shallow Water Offshore Wind Turbine." *Marine Structures* 70. https://doi.org/10.1016/j.marstruc.2019.102705.

[68] Wang, Shaofeng, Torben Juul Larsen, and Henrik Bredmose. 2021. "Ultimate Load Analysis of a 10 MW Offshore Monopile Wind Turbine Incorporating Fully Nonlinear Irregular Wave

Journal of Offshore Mechanics and Arctic Engineering. Received April 22, 2022;
Accepted manuscript posted August 22, 2022. doi:10.1115/1.4055402

Kinematics." *Marine Structures* 76. https://doi.org/10.1016/j.marstruc.2020.102922.

[69] Hirdaris, S. E., W. Bai, D. Dessi, A. Ergin, X. Gu, O. A. Hermundstad, R. Huijsmans, et al. 2014. "Loads for Use in the Design of Ships and Offshore Structures." *Ocean Engineering*. Pergamon. https://doi.org/10.1016/j.oceaneng.2013.09.012.

[70] Bachynski, Erin, Maxime Thys, and Virgile Delhaye. 2019. "Dynamic Response of a Monopile Wind Turbine in Waves: Experimental Uncertainty Analysis for Validation of Numerical Tools." *Applied Ocean Research* 89: 96–114. https://doi.org/10.1016/j.apor.2019.05.002.

[71] Darvishi-Alamouti, Saeed, Mohammad Reza Bahaari, and Majid Moradi. 2017. "Natural Frequency of Offshore Wind Turbines on Rigid and Flexible Monopiles in Cohesionless Soils with Linear Stiffness Distribution." *Applied Ocean Research* 68: 91–102. https://doi.org/10.1016/j.apor.2017.07.009.

[72] Veritas, Det Norske. 2010. "Environmental Conditions and Environmental Loads." *Dnv*, no. October: 9–123.

[73] Morison, J R, J W Johnson, and S A Schaaf. 1950. "The Force Exerted by Surface Waves on Piles." *Journal of Petroleum Technology* 2 (05): 149–54. https://doi.org/10.2118/950149-g.

[74] Bak, Christian, Frederik Zahle, Robert Bitsche, Taeseong Kim, Anderes Yde, Lars Christian Henriksen, Anand Natarajan, and Morten Hansen. 2013. "Description of the DTU 10 MW Reference Wind Turbine." https://dtu-10mw-rwt.vindenergi.dtu.dk.

[75] Zuo, Haoran, Kaiming Bi, and Hong Hao. 2018. "Dynamic Analyses of Operating Offshore Wind Turbines Including Soil-Structure Interaction." *Engineering Structures* 157 (February): 42–62. https://doi.org/10.1016/J.ENGSTRUCT.2017.12.001.

[76] Peder Hyldal Sørensen, Søren, and Lars Bo Ibsen. 2013. "Assessment of Foundation Design for Offshore Monopiles Unprotected against Scour." *Ocean Engineering* 63 (May): 17–25. https://doi.org/10.1016/J.OCEANENG.2013.01.016.

[77] Mathematica. 2021. "The World's Definitive System for Modern Technical Computing." https://www.wolfram.com/mathematica.

Journal of Offshore Mechanics and Arctic Engineering. Received April 22, 2022;
Accepted manuscript posted August 22, 2022. doi:10.1115/1.4055402

Table 1- Symbols definition

Symbol	**Structural properties**
L	Nacelle level from the seabed (m)
L_{Tow}	Tower length (m)
D_{Tow}	Tower average diameter (m)
t_{Tow}	Tower average thickness (m)
m_{Tow}	Tower mass of unit length (kg/m)
E_{Tow}	Tower Young's modulus (GPa)
EI_{Tow}	Flexural rigidity of the tower, i.e., $E_{Tow}I_{Tow}$ $(GPa.m^4)$
M_n	Nacelle-Rotor assembly mass (kg)
J_p	Nacelle-Rotor assembly rotational inertia (k$g.m^2$)
L_{Plat}	Platform level from the seabed (m)
D_{Mon}	Monopile average diameter (m)
t_{Mon}	Monopile average thickness (m)
A_{Mon}	Monopile cross-sectional area (m^2)
m_{Mon}	Monopile mass of unit length (kg/m)
E_{Mon}	Monopile Young's modulus (GPa)
EI_{Mon}	Flexural rigidity of the monopile, i.e., $E_{Mon}I_{Mon}$ $(GPa.m^4)$
ρ_s	Material Density (kg/m^3)
Symbol	**Support Stiffness**
K_L	Lateral stiffness (GN/m)
K_{LR}	Cross stiffness (GN)
K_R	Rotational stiffness $(GN.m)$
Symbol	**Hydrodynamic loading properties**
d	Water depth (m)
C_D	Drag coefficient
C_A	Added mass coefficient
C_M	Inertia coefficient
ρ_w	Sea water density (kg/m^3)
λ	Ocean wavelength (m)
H	Ocean wave height (m)

Journal of Offshore Mechanics and Arctic Engineering. Received April 22, 2022;
Accepted manuscript posted August 22, 2022. doi:10.1115/1.4055402

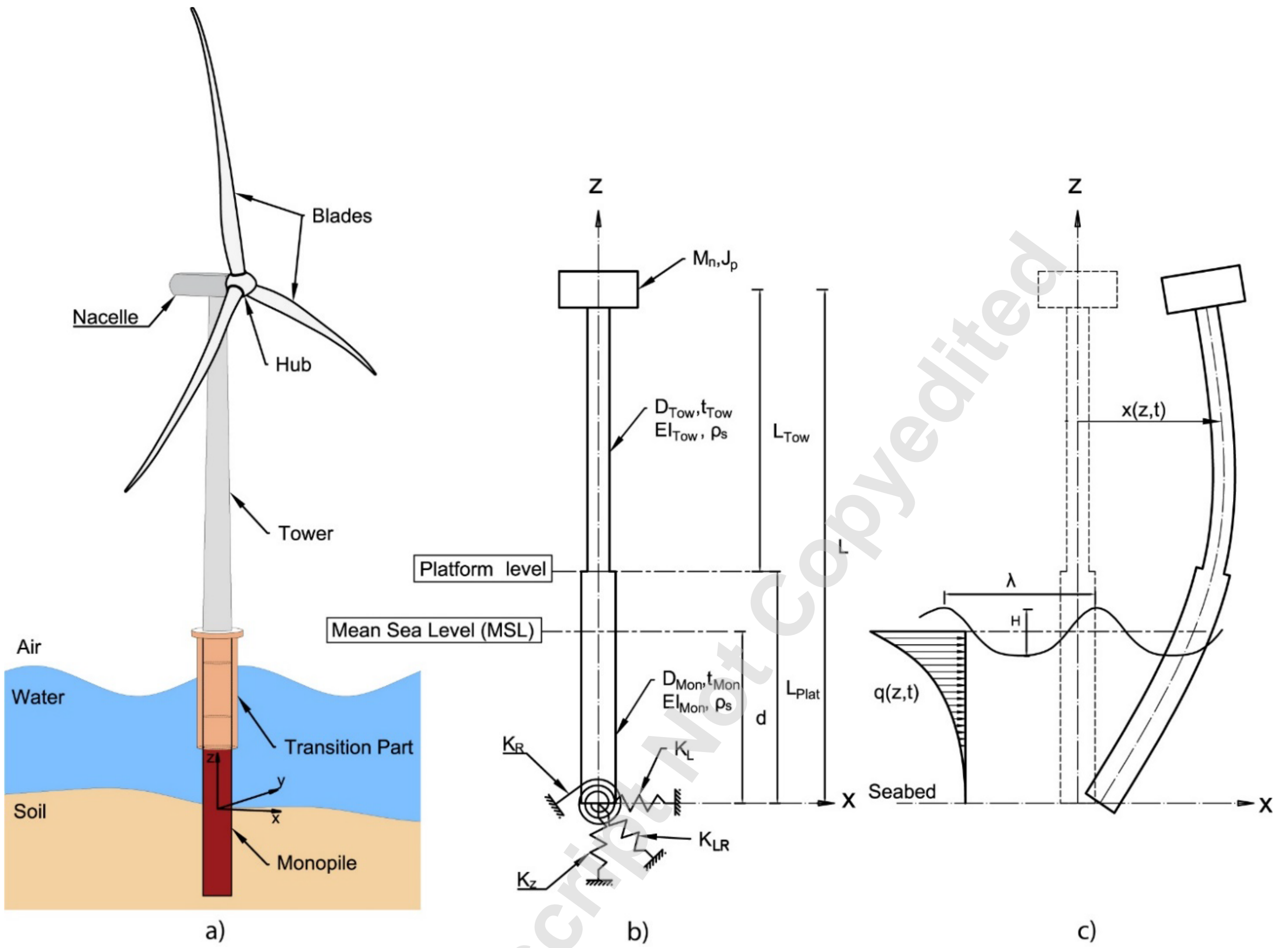

Figure 1- a) A typical OWT configuration, b) Schematic of the model, c) wave loading direction and system coordinates

Table 2- DTU 10 MW OWT structural properties [74]

	Symbol	Value
Tower length (m)	L_{Tow}	119
Tower average diameter (m)	D_{Tow}	9.6
Tower average thickness (m)	t_{Tow}	0.0295
Tower Young's modulus (GPa)	E_{Tow}	210
Nacelle-Rotor assembly mass (kg)	M_n	676723
Nacelle-Rotor assembly rotational inertia (kg.m2)	J_p	1.7 x 10^8
Platform level from mudline (m)	L_{Plat}	45
Monopile average diameter (m)	D_{Mon}	8.3
Monopile average thickness (m)	t_{Mon}	0.09
Monopile Young's modulus (GPa)	E_{Mon}	210
Material density (kg/m3)	ρ_s	8500

Journal of Offshore Mechanics and Arctic Engineering. Received April 22, 2022;
Accepted manuscript posted August 22, 2022. doi:10.1115/1.4055402

Table 3- Hydrodynamic loading properties

	Symbol	Value
Water depth (m)	d	35
Drag coefficient	C_D	0.65
Added mass coefficient	C_A	1
Inertia coefficient	C_M	2
Sea water density (kg/m3)	ρ_w	1025

Table 4- The values of the coupled springs [60]

	Symbol	Value
Lateral stiffness (GN/m)	K_L	2.48
Cross stiffness (GN)	K_{LR}	-20.7
Rotational stiffness (GN.m)	K_R	412

Table 5- Solution variables

d/l	a_{Tow}	a_{MA}	a_{MU}	α_1	α_2	α_3	α_4	α_5	α_6	γ_{AT}	γ_{UT}
0.227	12125	14585	7501	5.84E-04	-4.88E-03	0.097	0.188	1.59E-04	8.48E-07	0.911	1.271

Table 6- *The natural mode frequencies of the system with and without the effect of added mass*

Mode Number	f_n (Hz)		Difference (%)
	No added mass	Added mass	
1	0.166561	0.166393	-0.1
2	1.13463	1.0322	-9.0
3	2.3888	1.98416	-16.9
4	4.3686	3.8174	-12.6
5	8.025	6.593	-17.8
6	12.198	9.8905	-18.9

Journal of Offshore Mechanics and Arctic Engineering. Received April 22, 2022;
Accepted manuscript posted August 22, 2022. doi:10.1115/1.4055402

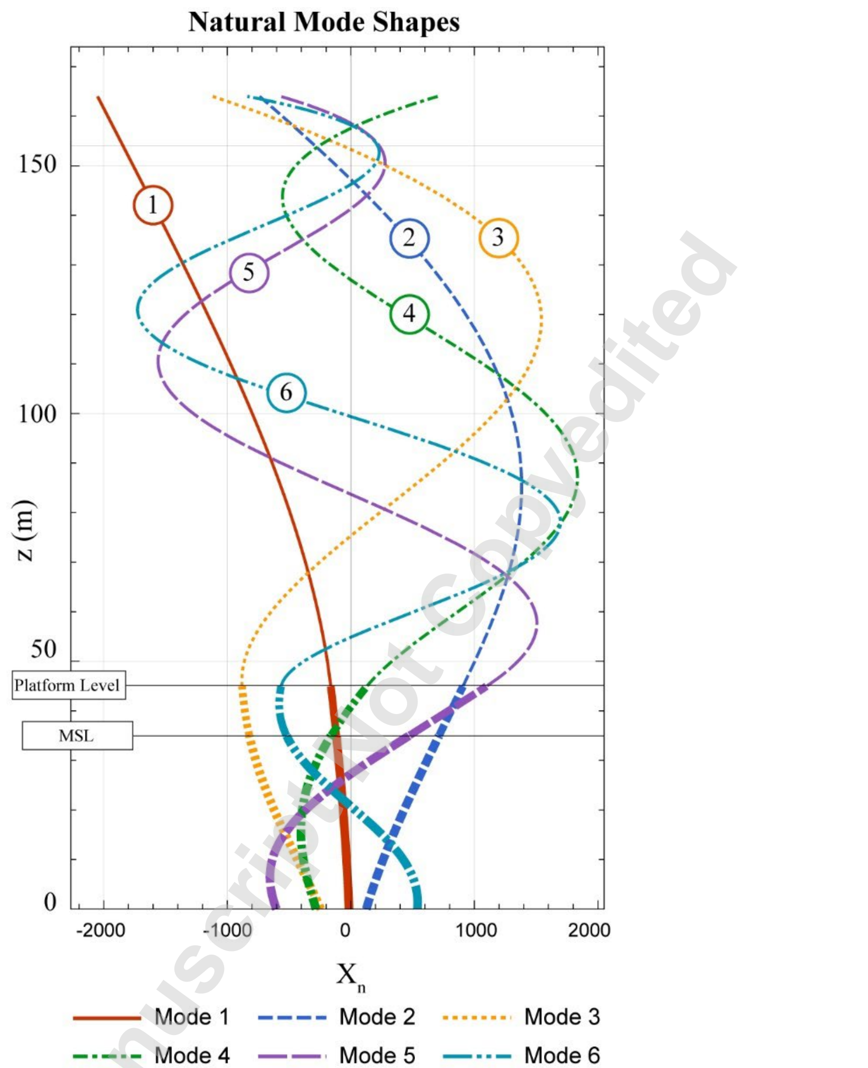

Figure 2- The normalized natural mode shapes of the system with the added mass (MSL=Mean Sea Level)

Journal of Offshore Mechanics and Arctic Engineering. Received April 22, 2022;
Accepted manuscript posted August 22, 2022. doi:10.1115/1.4055402

Table 7- *Comparison of the 1st natural frequency between the proposed method and full 3D FE-based model by* [60]

Water depth (m)	Platform level (m)	Monopile outer diameter (m)	Monopile thickness (cm)	1st Natural Frequency (Hz)		Deviation (%)
				Alkhoury et al. [60]	Proposed Model	
25	35	8.3	9	0.2009	0.1731	-13.8
			10	0.202	0.1743	-13.7
			12	0.2056	0.1771	-13.9
		9	10	0.2074	0.177	-14.7
			12	0.2112	0.1795	-15.0
			14	0.2158	0.1813	-16.0
		10	11	0.2177	0.1809	-16.9
			13	0.2186	0.1828	-16.4
			15	0.2207	0.1837	-16.8
35	45	8.3	9	0.1909	0.1663	-12.9
			10	0.1928	0.1682	-12.8
			12	0.197	0.171	-13.2
		9	10	0.1992	0.1719	-13.7
			12	0.2038	0.1734	-14.9
			14	0.2092	0.176	-15.9
		10	11	0.2096	0.1768	-15.6
			13	0.2129	0.1784	-16.2
			15	0.2155	0.1795	-16.7
45	55	8.3	9	0.1811	0.1592	-12.1
			10	0.1836	0.1614	-12.1
			12	0.189	0.1648	-12.8
		9	10	0.1909	0.1658	-13.1
			12	0.1962	0.1686	-14.1
			14	0.2023	0.1708	-15.6
		10	11	0.203	0.1717	-15.4
			13	0.207	0.1736	-16.1
			15	0.2101	0.175	-16.7

Journal of Offshore Mechanics and Arctic Engineering. Received April 22, 2022;
Accepted manuscript posted August 22, 2022. doi:10.1115/1.4055402

Table 8- The range of solution variables used for the parametric study and the equality to the parameters

Solution variable	Equivalent to
$\alpha_1 = \infty$	$K_L = \infty$
$\alpha_2 = 0$	$K_{LR} = 0$
$0.2 < \alpha_3 < \infty$	$271\ (GN.m) < K_R < \infty$
$\alpha_4 = 1$	$EI_{Mon} = EI_{Tow} = 1357\ GN.m^2$
$0 < \alpha_5 < 10^{-3}$	$0 < J_P < 1.35 \times 10^9\ Kg.m^2$
$0 < \alpha_6 < 10^{-6}$	$0 < M_n < 1357\ ton$
$\gamma_{AT} = 1$	$A_{Mon} = A_{Tow}$
$\gamma_{UT} = 1.36$	See Eq. (62)

969
970

Journal of Offshore Mechanics and Arctic Engineering. Received April 22, 2022;
Accepted manuscript posted August 22, 2022. doi:10.1115/1.4055402

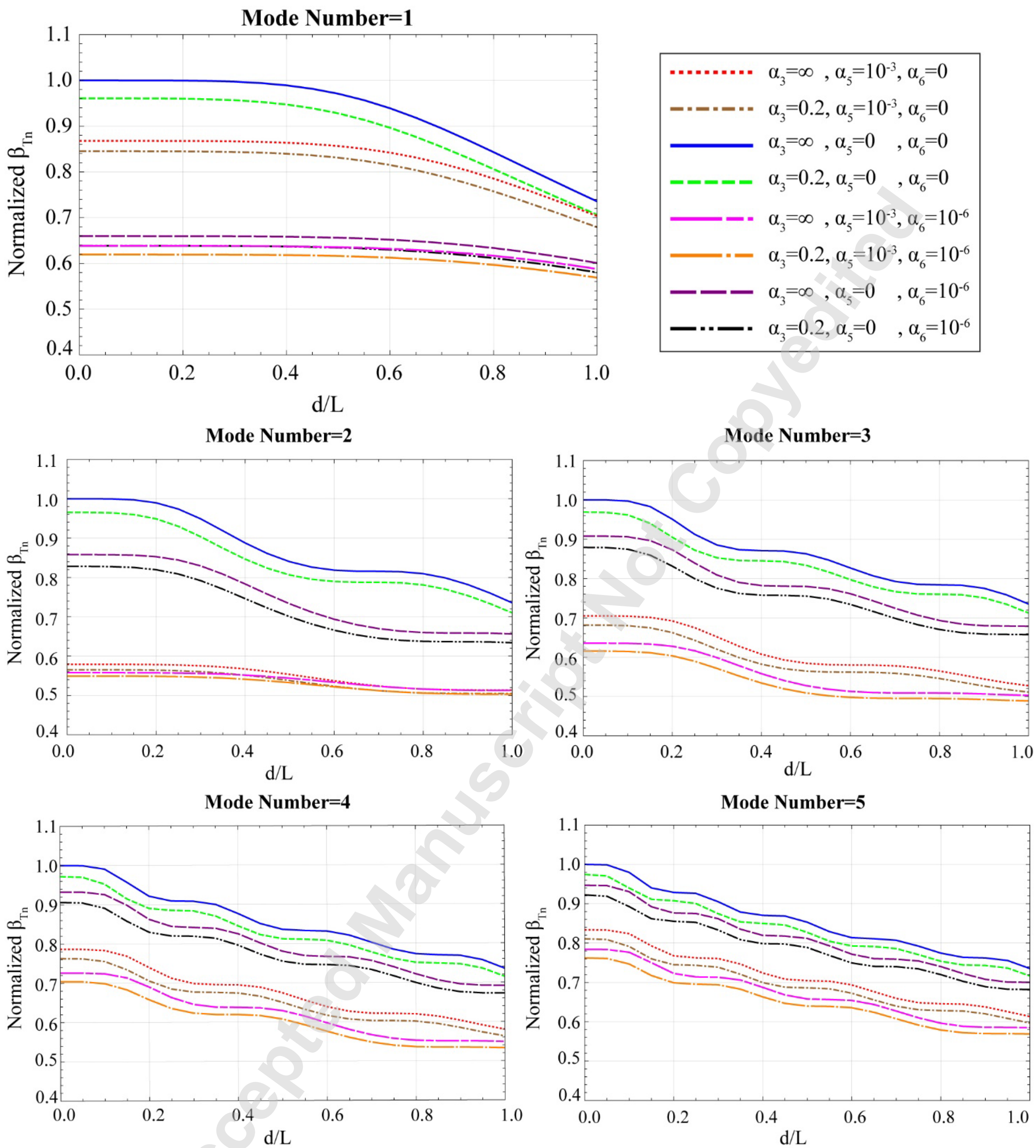

Figure 3- Variation of system's wavenumber, β_{Tn}, for different values of the water depth ratio, d/L, in the first 5 modes

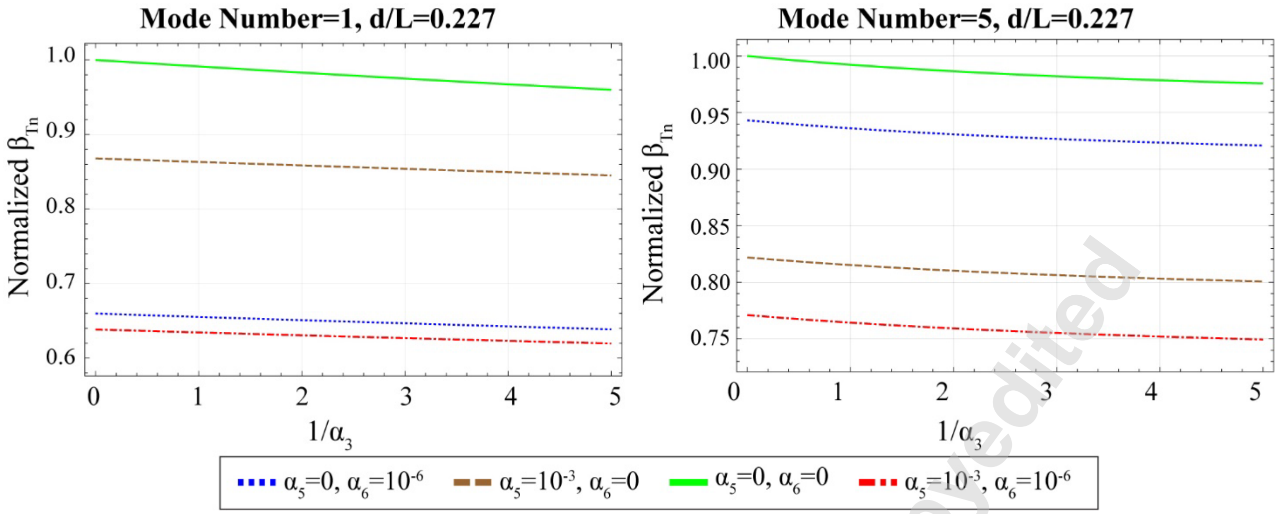

Figure 4- Variation of normalized wavenumber of the system for the above water section, β_{Tn}, for different values of α_3 in the 1st and 5th modes.

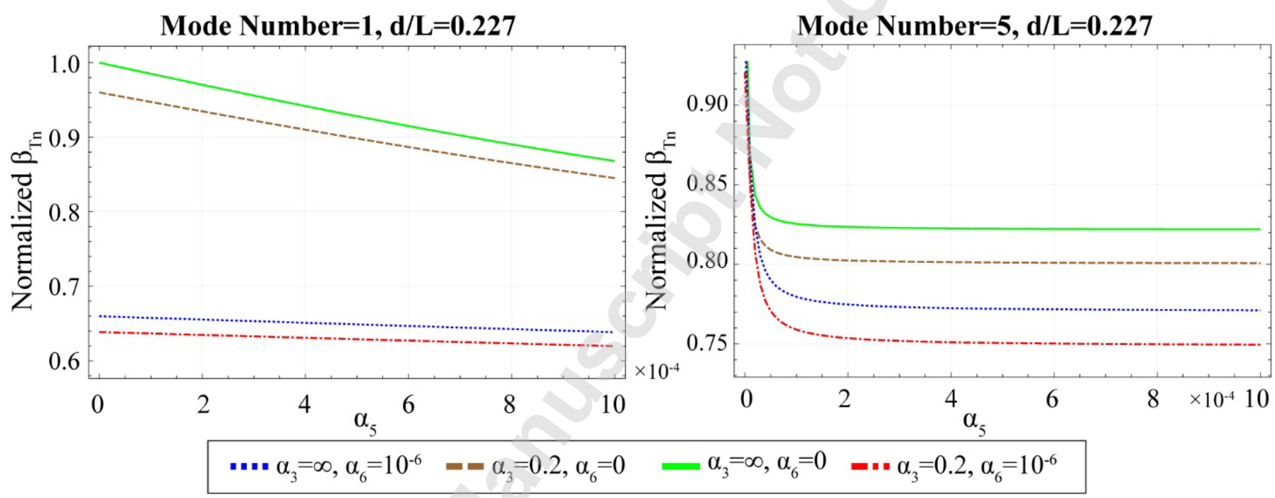

Figure 5- Variation of normalized wavenumber of the system for the above water section, β_{Tn}, for different values of α_5 in the 1st and 5th modes.

Journal of Offshore Mechanics and Arctic Engineering. Received April 22, 2022;
Accepted manuscript posted August 22, 2022. doi:10.1115/1.4055402

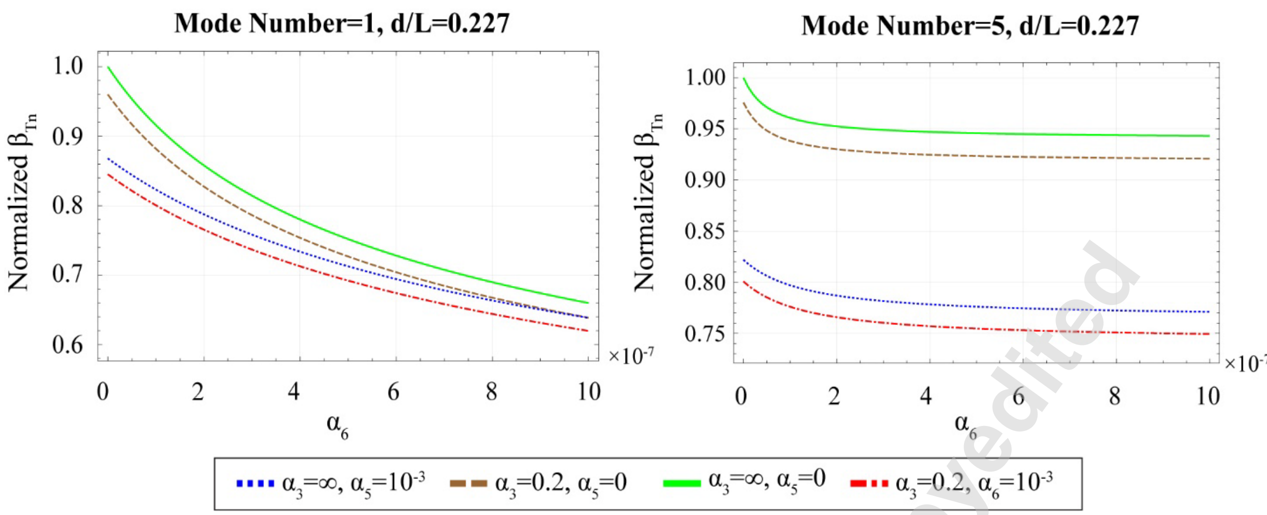

Figure 6- Variation of normalized wavenumber of the system for the above water section, β_{Tn}, for different values of α_6 in the 1st and 5th modes.

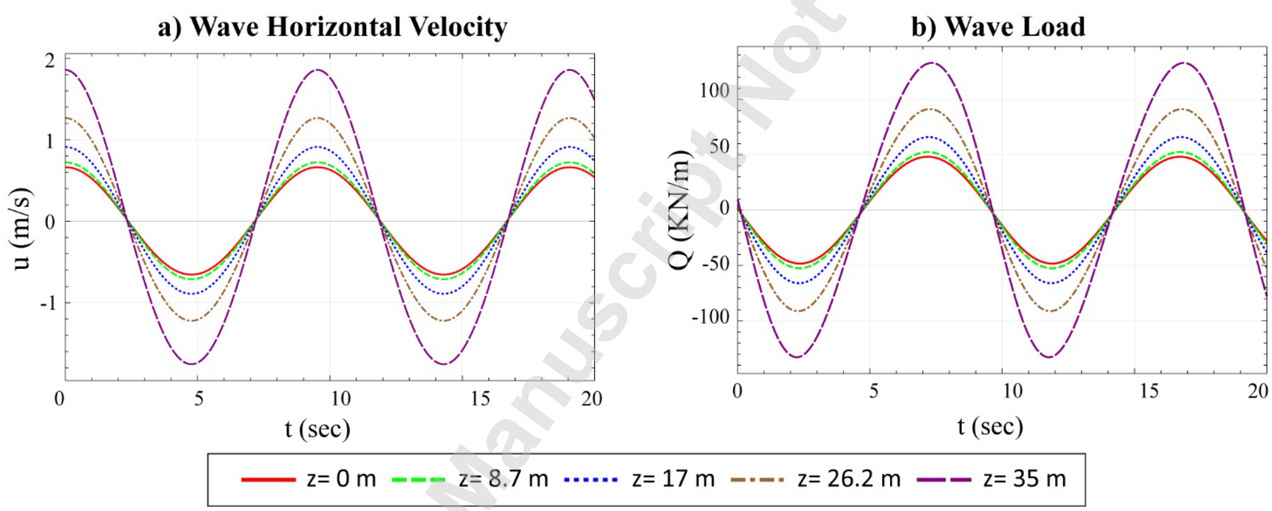

Figure 7- a) The wave horizontal particle velocity, and b) wave load obtained from Morison's equation, for H=5.1 m and λ=132m.

Table 9- Specification of the ocean wave applied to the reference tower

Height H (m)	Ocean wavelength λ (m)	Water depth d (m)	Frequency f (Hz)	Period T (sec)	$\frac{H}{gT^2}$	$\frac{d}{gT^2}$	$\frac{H}{d}$	Ursell Number Ur
5.1	132	35	0.105	9.53	0.00572	0.0392	0.145	2.072

Journal of Offshore Mechanics and Arctic Engineering. Received April 22, 2022;
Accepted manuscript posted August 22, 2022. doi:10.1115/1.4055402

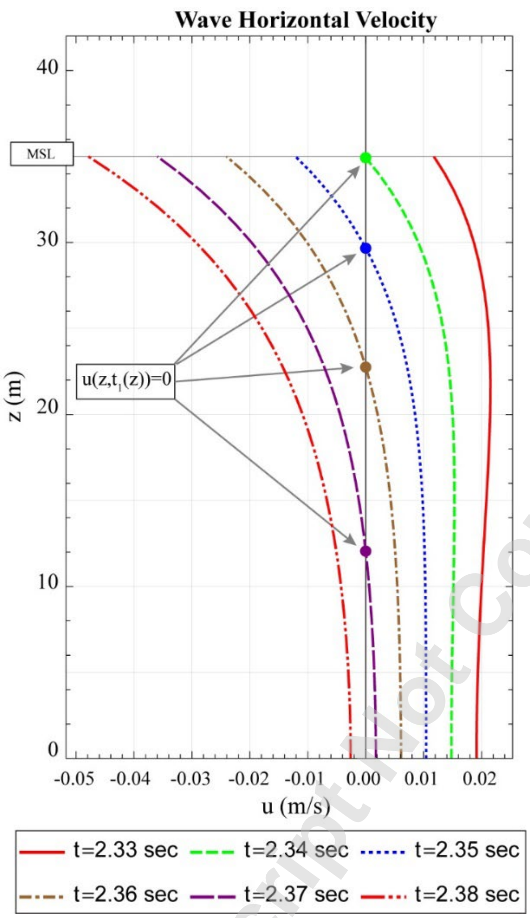

Figure 8- The variation of the wave horizontal particle velocity at around $t_1(z)$, for wave with $H = 5.1\ m$ and $\lambda = 132\ m$.

981

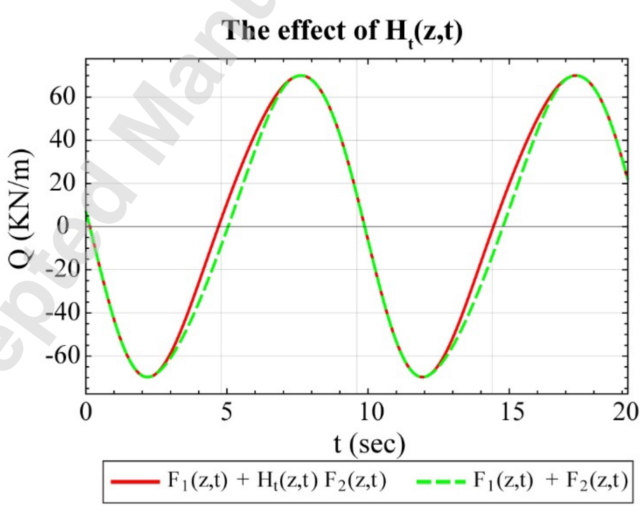

Figure 9- The effect of the term $H_t(z,t)$ in Morison's formula with the 2nd order wave kinematics for $H = 5.1\ m$ and $\lambda = 132\ m$ at z=35 m.

982
983

Journal of Offshore Mechanics and Arctic Engineering. Received April 22, 2022;
Accepted manuscript posted August 22, 2022. doi:10.1115/1.4055402

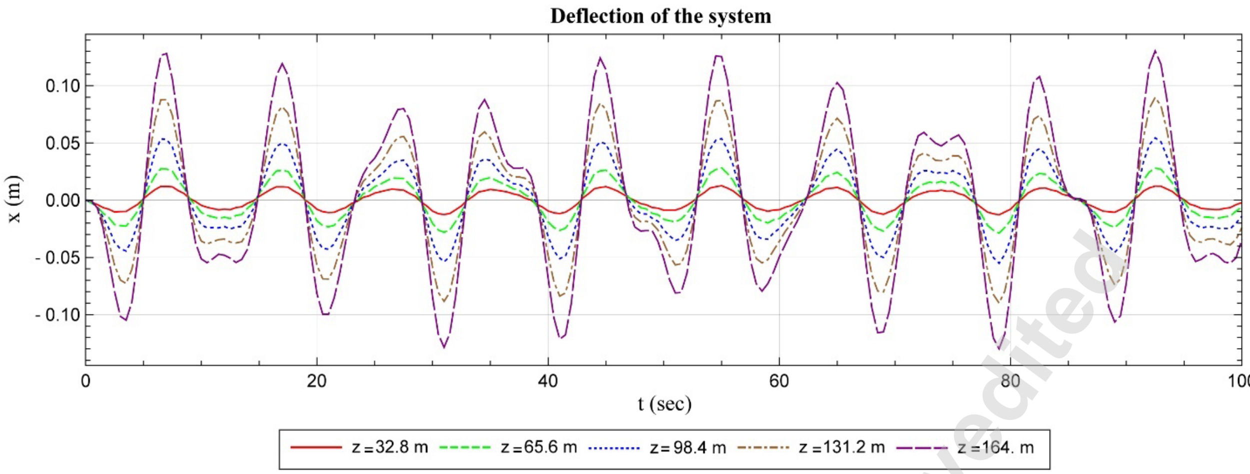

Figure 10- The response of the reference tower at different heights.

984

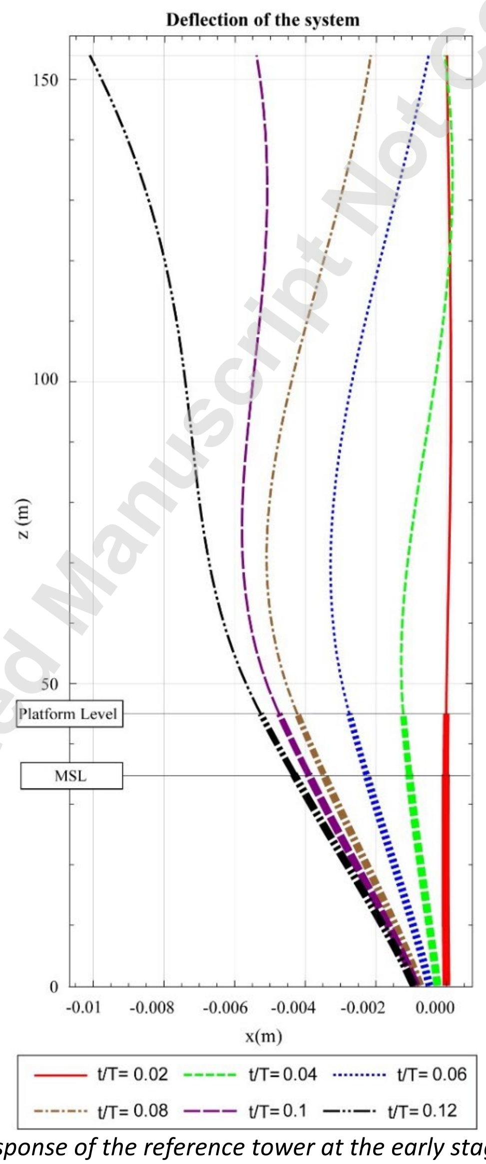

Figure 11- The response of the reference tower at the early stages of the motion.

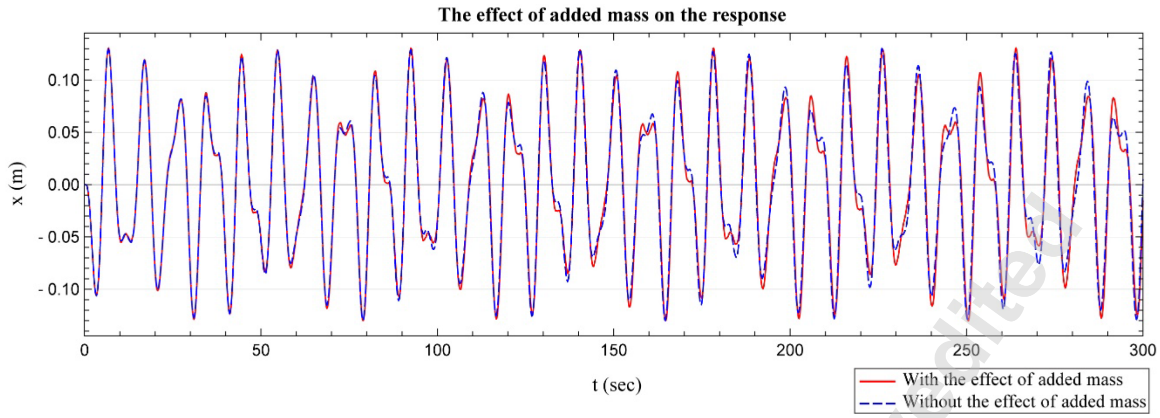

Figure 12- Comparison between the response of the tower at the hub level with and without the added mass.

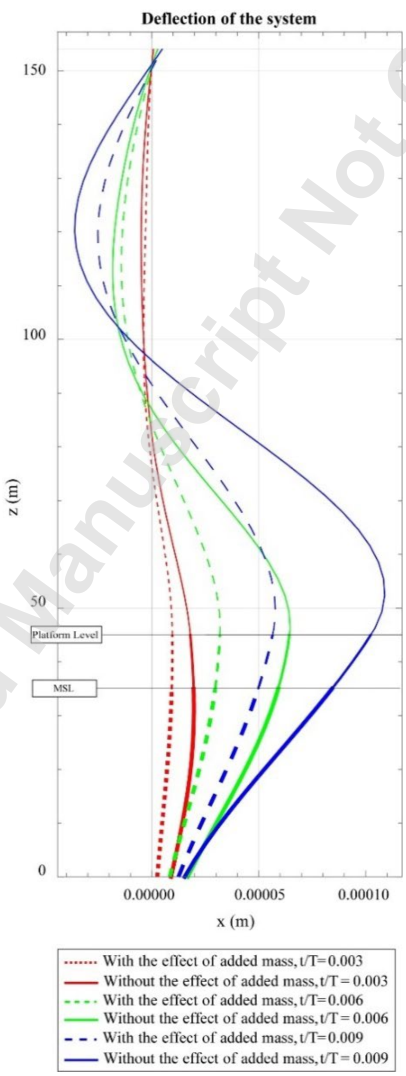

Figure 13- Comparison between the response of the reference tower with and without the added mass at early stages of the motion

Journal of Offshore Mechanics and Arctic Engineering. Received April 22, 2022;
Accepted manuscript posted August 22, 2022. doi:10.1115/1.4055402

Table 10-The properties of an OWT for the numerical comparison

Structural properties	**Symbol**	**Value**	**Support Stiffness**	**Symbol**	**Value**
Tower length (m)	L_{Tow}	70	Lateral stiffness (GN/m)	K_L	∞
Tower average diameter (m)	D_{Tow}	6	Cross stiffness (GN)	K_{LR}	0
Tower average thickness (m)	t_{Tow}	0.045	Rotational stiffness (GN.m)	K_R	205.72
Tower Young's modulus (GPa)	E_{Tow}	210			
Nacelle-Rotor assembly mass (kg)	M_n	0	**Hydrodynamic loading properties**	**Symbol**	**Value**
Nacelle-Rotor assembly rotational inertia (kg.m2)	J_p	0	Water depth (m)	d	30
Platform level from mudline (m)	L_{Plat}	45	Drag coefficient	C_D	0.65
Monopile average diameter (m)	D_{Mon}	6	Added mass coefficient	C_A	1
Monopile average thickness (m)	t_{Mon}	0.045	Inertia coefficient	C_M	2
Monopile Young's modulus (GPa)	E_{Mon}	210	Sea water density (kg/m3)	ρ_w	1020
Material Density (kg/m3)	ρ_s	7820			

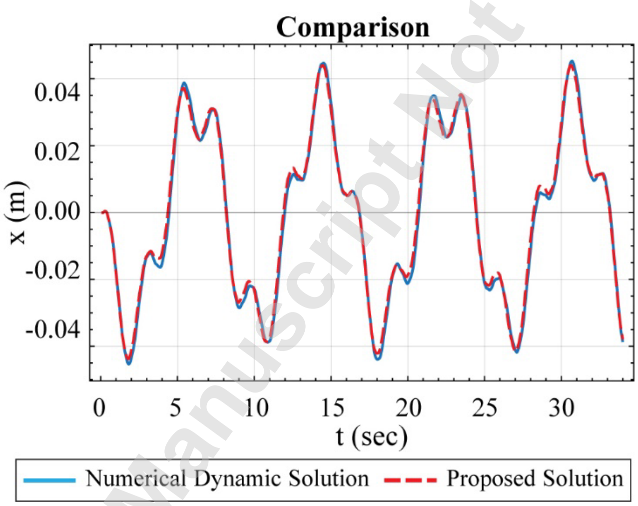

Figure 14- Comparison of the results of the proposed solution with the numerical one at z=115 m.